Part I
Principles

1
The Spallation Process

1.1
Historic Remarks and Definitions

There is no generally accepted definition of the term ''spallation reaction'' although this type of nuclear reaction is observed in astrophysics, geophysics, radiotherapy, radiobiology, and at all applications together with accelerators. Cosmic ray physicists refer still to such reactions induced by cosmic rays as ''fragmentation.'' But for all practical purposes, spallation refers to nonelastic nuclear reactions that occur when energetic particles, for example, protons, neutrons, or pions interact with an atomic nucleus. So at least one of the two collision partners is a complex nucleus in which the available energy exceeds the interaction energy between nucleons in the nucleus. Thus, a nucleon–nucleus or pion–nucleus or nucleus–nucleus reaction, in which the incident energy exceeds some 10th of MeV per a.m.u. is referred to as spallation or spallation reaction. The term comes from the verb ''to spall,'' meaning to chip with a hammer [1]. There is no clear separation of spallation from the lower energy nuclear reactions. One type may merge into the other as the energy of the incident particle increases.

(a) A definition found in *Encyclopedia Britannica*: ''Spallation is a high-energy nuclear reaction in which a target nucleus struck by an incident (bombarding) particle of energy greater than about 50 million electron volts (50 MeV) ejects numerous lighter particles and becomes a product nucleus correspondingly lighter than the original nucleus. The light ejected particles may be neutrons, protons, or various composite particles equivalent.''

(b) A definition for spallation to be specified in the context of accelerator driven systems or high-intensity neutron sources is ''the disintegration of a nucleus by means of high energetic proton-induced reactions. Typically approximately 20 neutrons are created per incident GeV proton.''

(c) A much shorter definition: ''Spallation is a nonelastic nuclear interaction induced by a high-energy particle $\geq$50 MeV producing numerous secondary particles.''

The following terminology is used here for clarification to describe the high-energy nuclear processes. The terms ''inelastic,'' ''quasielastic,'' ''absorption,'' and ''nonelastic'' describe usually reactions which are not pure elastic scattering from the nucleus as a whole. Absorption is in general used to describe all nonelastic

Handbook of Spallation Research: Theory, Experiments and Applications. Detlef Filges and Frank Goldenbaum

ISBN: 978-3-527-40714-9

events when an optical analysis is made. The term inelastic is used in describing low-energy phenomena where scattered particles hold their identity but leave the nucleus in an excited state. The term ''nonelastic'' is used to describe all events which are not elastic scattering with the nucleus as a whole (see also page 44).

Historically the idea of the basic reaction mechanism – the intranuclear cascade – was first proposed by Serber [2]. He suggested that at energies of about 100 MeV, the deBroglie wavelength of the incident particle becomes comparable to, or shorter than, the average internucleon distance within the nucleus 10^{-13} cm. That is the collision time between the incident particle and a nucleon inside the nucleus becomes short compared to the time between nucleon collisions inside the nucleus. Goldberger [3] was the first to perform calculations using Serbers's model approach. (It was reported that two people working for 2 weeks were able to generate 100 Monte Carlo particle histories by hand calculations.) Metropolis et al. [4, 5] were the first to report extensive calculations using computers and generated large amounts of data for incident particles <400 MeV below the pion threshold. Also Dostrovsky et al. [6, 7] studied by Monte Carlo simulation the systematics known as nuclear evaporation [8, 9] programmed first for the Los Alamos MANIAC computer during the 1950s (see Section 2.2).

Since then, numerous refinements and extensions of the spallation models have been made in relation with experiments and nowadays with the development of spallation neutron sources. During the 1960s primarily three groups were active: Barashenkov et al. at Dubna [10], Chen et al. at BNL [11], and Bertini et al. at ORNL [12]. These groups had also studied numerical comparisons of results from the models as investigated by these three groups for low-energy protons at energies of 150 and 300 MeV [13]. Details of this early research will be discussed in Chapter 2. Still the most important physics uncertainty associated with the predicting the interaction of high-energy particles such as hadrons, leptons, and pions with matter lies in determining the description – multiplicities and energy and angular distributions – of particles produced in nonelastic nuclear collisions.

Much of the research on spallation consists in experiments to measure cross sections. The early experiments were using cosmic rays as incident particles. But nowadays extensive experiments are done at high-energy accelerators also in connection with the development of high-intensity neutron spallation sources in the last 20 years. Very often the target in question is not a single nucleus. If it is not a ''thin'' target, where no secondary reactions are occurring, but a rather ''thick'' target further secondary reactions will arise and a so-called nuclear cascade will be produced within the ''thick'' target. Thick targets can be found in nature, e.g., meteoroids, the moon's surface, the martian's surface, the earth's atmosphere, the earth itself, or the human body. The transport of cosmic rays through the earth's atmosphere [14] is a good example of a nuclear cascade (see Section 1.2). Spallation will take place wherever a flux of high-energy particles collides with some matter. There are two main types of high-energy particles in the universe: cosmic rays and particles from accelerators. The bombardment of matter with high-energy particles produces not only spallation but also a rather complex sequence of nuclear and atomic interactions, which will be discussed in detail in Section 1.3. In Figure 1.1,

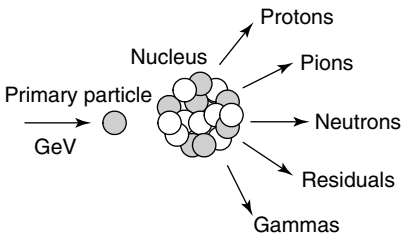

Fig. 1.1 Generalized possible particle production of a particle–nucleus interaction in the GeV energy range.

a scheme of a more generalized possible particle production on a particle–nucleus interaction is depicted.

1.2 Spallation by Cosmic Ray-Induced Reactions

From experiments around 1912/1913, Hess found in free balloon flights to an altitude of about 5300 m that there exists a radiation within the earth's atmosphere of very great penetration power. Hess received the Nobel Prize for this discovery in 1936. It was concluded that these rays were of cosmic origin. They were referred to as "Höhenstrahlung," which might be translated as "high altitude rays." It is now common to speak of *cosmic rays*. The primary rays in outer space are relatively simple, but interaction with matter changes their nature as they pass through the atmosphere. Galactic cosmic rays or galactic cosmic radiation (GCR) consist of high-energy particles believed to propagate throughout all the space and to originate both within and outside our galaxy. The measured cosmic ray energy spectra of galactic protons, helium ions, carbon ions, and iron ions are shown in Figure 1.2.

The primary cosmic ray flux in the solar system at the earth's orbit is a mixture of energetic protons, alpha particles, and a small mixture of heavier nuclei as shown in Figure 1.2. This flux and its composition vary over the 11-year solar activity cycle. After passing the interplanetary medium and the geomagnetic field, the primary cosmic rays propagate by means of a nucleonic cascade through the atmosphere. More details of the principal interactions by cosmic rays in the atmosphere and the produced energy spectra, the solar wind distribution, and trapped spectra by the geomagnetic field may be seen in [15, 17–19]. Formulas (1.1) also show the general reaction mechanisms.

Secondary cosmic rays include pions which decay in muons, neutrinos, and gamma rays, as well electrons and positrons by muon decay and gamma ray interaction with the earth's atmosphere. The most abundant secondary cosmic rays reaching the earth's surface are muons (see Figure 1.4), with an average intensity of about 100 per m^2. In Table 1.1 some basic properties of pions, kaons, and muons are summarized. More details are given in the "Review of Particle

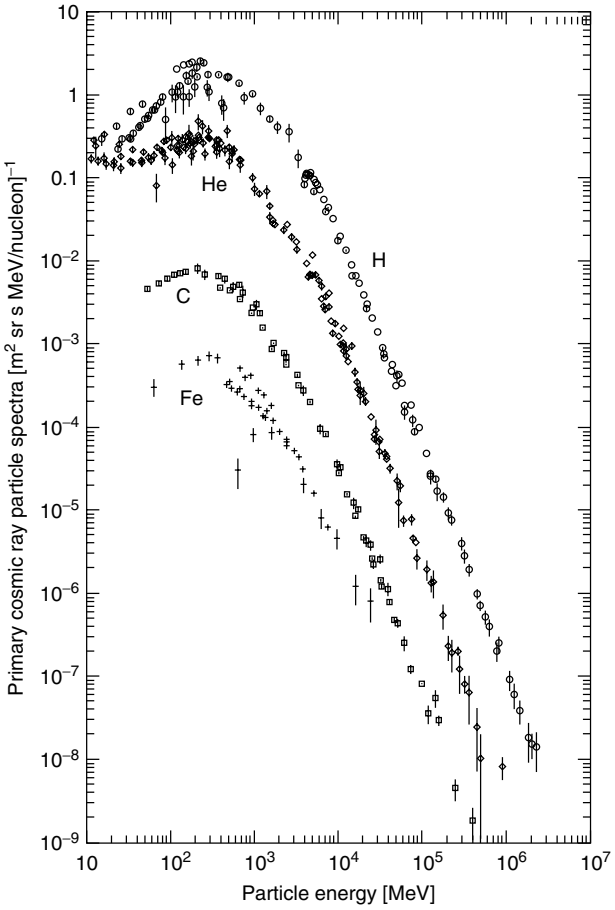

Fig. 1.2 Cosmic ray energy spectra measured at the orbit of the earth (1 AU = astronomical unit = mean distance between the Sun and the Earth) for hydrogen, helium, carbon, and iron (taken from Simpson [15, 16]).

Tab. 1.1 Some basic particle properties of pions, kaons, and muons.

Particle	Symbol	Rest mass (MeV/c^2)	Mean lifetime (s)
Charged pions	$\pi^{\pm}$	139.6	2.60×10^{-8}
Neutral pions	π^{0}	134.0	0.84×10^{-16}
Charged kaons	$k^{\pm}$	493.7	1.24×10^{-8}
Neutral kaon	k^{0}	497.7	Weak decay
Charged muons	$\mu^{\pm}$	105.7	2.20×10^{-6}

Physics" of the Particle Data Group (PDG) [19] in Section 1.3.5.1 on page 23 in this book.

$$
\begin{aligned}
\mathrm{p} + \mathrm{air} &\longrightarrow \mathrm{p} + \mathrm{n} + \pi^{\pm} + \pi^{0} + \mathrm{k}^{\pm} + \mathrm{k}^{0},\\
n + \mathrm{air} &\longrightarrow \mathrm{p} + \mathrm{n} + \pi^{\pm} + \pi^{0} + \mathrm{k}^{\pm} + \mathrm{k}^{0},\\
\pi^{+} &\longrightarrow \mu^{+} + \nu_{\mu},\\
\pi^{-} &\longrightarrow \mu^{-} + \overline{\nu}_{\mu},\\
\mu^{-} &\longrightarrow \mathrm{e}^{-} + \overline{\nu}_{e} + \nu_{\mu},\\
\mu^{+} &\longrightarrow \mathrm{e}^{+} + \nu_{e} + \overline{\nu}_{\mu},\\
\mu^{\pm} &\text{ also inducing electromagnetic showers,}\\
\pi^{0} &\longrightarrow 2\gamma \longrightarrow \text{electromagnetic showers,}\\
\mathrm{k}^{+} &\longrightarrow \mu^{+}\nu_{\mu}, \quad \text{or}\\
&\qquad \pi^{+}\pi^{0}\\
&\qquad \pi^{+}\pi^{+}\pi^{-}\\
&\qquad \pi^{+}\pi^{0}\pi^{0}\\
&\qquad \pi^{0}\mathrm{e}^{+}\nu_{e}\\
&\qquad \pi^{0}\mu^{+}\nu_{\mu}.
\end{aligned}
\tag{1.1}
$$

The branches of the cosmic ray atmospheric propagation process are shown in Figure 1.3. The kaon contribution is small. In the vicinity of the earth's orbit, the composition of cosmic radiation is approximately 85% protons, 12% alpha particles, 1% nuclei of atomic numbers $Z > 2$, and 2% electrons and positrons [16]. At high energies above several GeV the spectra shown in Figure 1.2 could be well represented within interstellar space by a power-law energy dependence:

$$\phi_i \propto 1.8(E/A)^{-\gamma}[\text{nucleons}/(\text{cm}^2\ \text{s sr GeV})], \tag{1.2}$$

with ϕ_i the differential flux of element i at kinetic energy per nucleon (E/A) including rest mass energy and γ is in the range 2.5 to 2.7. The relative fractions of the primary and secondary incident nuclei are listed in Table 1.2.

The spectra distributions at 1 AU of particles with $A \leq 4$ are quite similar if the energies are taken per nucleon (E/A). They are characterized by a broad maximum of the differential spectrum between 100 and 1 GeV/A, and decrease by a power law for higher energies. Below ~10 GeV/nucleon the spectra are effected by solar modulation or the solar magnetic field [17]. Galactic radiation arriving within the heliosphere is isotropic. The spectra of nuclei extend to energies in excess of about 10^{20} eV.

Figure 1.4 shows the vertical fluxes and spectra of the major cosmic ray components in the atmosphere. Except for protons and electrons near the top of the atmosphere, all particles are produced in interactions of the primary cosmic rays with the air. Muons and neutrinos are products of the decay of charged mesons, while electrons and photons originate in decays of neutral mesons. Most of the measurements are made at ground level or near the top of the atmosphere.

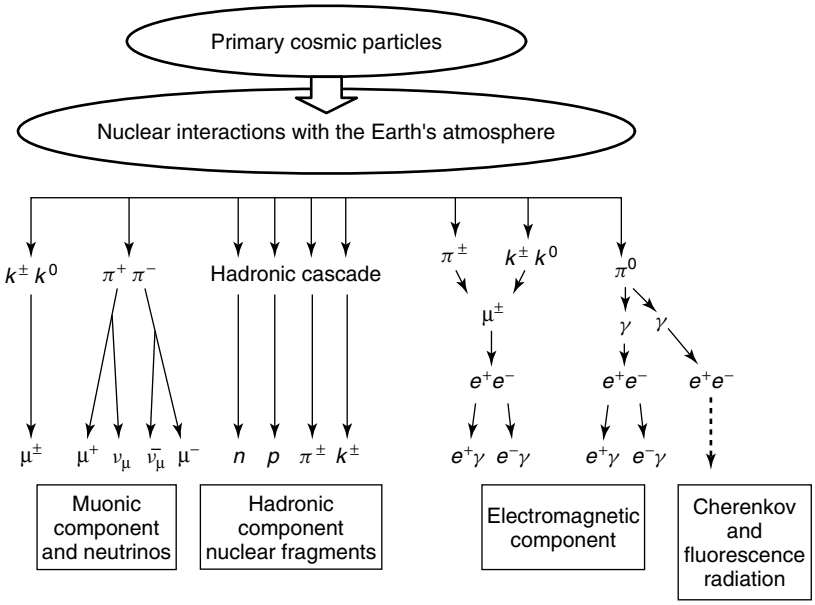

Fig. 1.3 The development of the components of cosmic rays propagating in the earth's atmosphere with kaon branches shown.

Tab. 1.2 Ratios of relative abundances of cosmic ray nuclei at 10.6 (GeV/nucleon) normalized to oxygen (≡1) with an oxygen flux of 3.26×10^{-6} ($cm^{-2}\ s^{-1} sr^{-1} (MeV/nucleon)^{-1}$) (see Ref. [20]).

Z	Element	Abundance ratio	Z	Element	Abundance ratio
1	H[a]	540	13–14	Al–Si	0.19
2	He[a]	26	15–16	P–S	0.03
3–5	Li–Be	0.40	17–18	Cl–Ar	0.01
6–8	C–O	2.20	19–20	K–Ca	0.02
9–10	F–Ne	0.30	21–25	Sc–Mn	0.05
11–12	Na–Mg	0.22	26–28	Fe–Ni	0.12

[a] The hydrogen and helium abundances are from [21].

According to [26] the modulated differential GCR proton flux can be described by the following formula:

$$\Phi(E_p, M) = C_p \cdot \frac{E_p(E_p + 2m_pc^2)(E_p + m + M)^{-2.65}}{(E_p + M)(E_p + 2mc^2 + M)} \quad \left(\mathrm{cm}^{-2}\,\mathrm{s}^{-2}\,\mathrm{MeV}^{-1}\right) \quad (1.3)$$

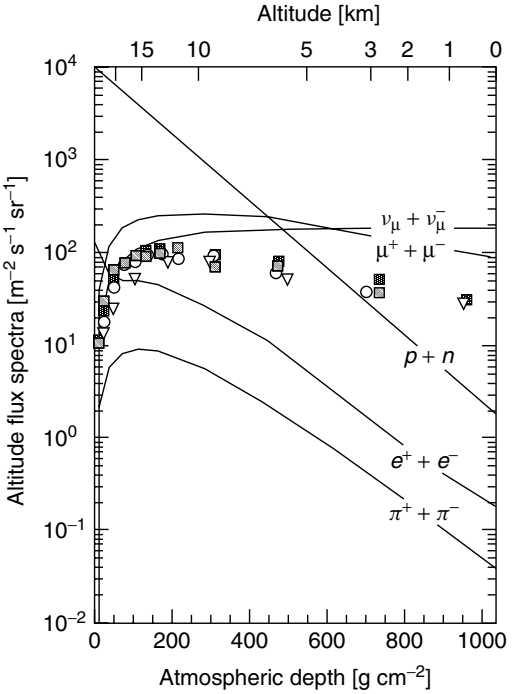

Fig. 1.4 Vertical fluxes and spectra of cosmic rays in the atmosphere with energy E > 1 GeV estimated from the nucleon flux of formula 1.2 (see also [19]). The symbols show measurements of negative muons with energy $E > 1$ GeV [22–25].

with $m = 780 \cdot \exp(-2.5 \times 10^{-4} \cdot E_p)$, and the normalization factor $C_p = 1.24 \times 10^6$ ($cm^{-2}\, s^{-1}\, MeV^{-1}$), $m_p = 938.3(MeV\, c^{-2})$ the proton rest mass, c the velocity of light, E_p the proton energy in (MeV), and M (MeV) the modulation parameter of the sun.

The solar modulation parameter M varies with the 11-year solar cycle. As shown in [26], small modulation parameters are typical for spectra during times of a quiet sun – 1965 $M = 450$ MeV and 1977 $M = 300$ MeV–, large modulation parameters for an active sun – 1969 $M = 900$ MeV. For the simulation of present-day irradiation processes, the arithmetic mean GCR spectrum from solar minimum (1965) with $M = 450$ MeV and solar maximum (1969) with $M = 900$ MeV may be adequate [27]. This spectrum is equivalent to a GCR spectrum with $M = 675$ MeV. An example for different values of M is shown in Figure 1.5 using formula (1.3) of [26].

The elemental composition of cosmic rays is an active area of research since the relative abundances provide tests of theories on the origin of the elements, or nucleosynthesis. Figure 1.6 shows the relative abundances of all elements at a typical energy of 2 GeV/nucleon. In radiation effect assessments, it is common to consider the cosmic ray ions in three groups:

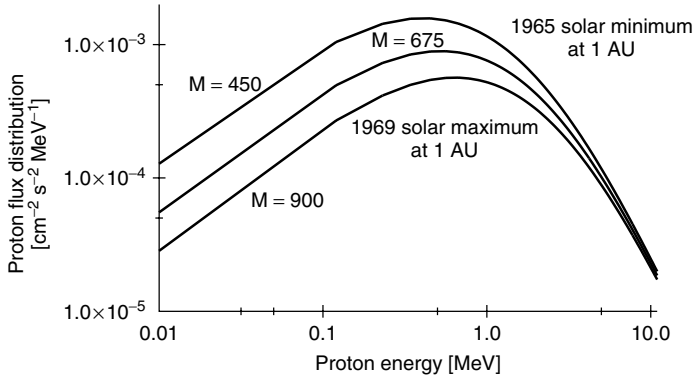

Fig. 1.5 Comparison of GCR cosmic ray spectra with different modulation parameters $M = 450$, 675, 900 MeV at 1 AU. (1 AU $\equiv$ 1 astronomical unit $= 1.49 \times 10^{13}$ cm, the mean distance between the earth and the sun).

- H and He,
- HZE ions (i.e., high charge number Z, and high-energy loss E, which includes ions having $Z \leq 30$),
- ultraheavy cosmic rays $Z > 30$.

Since energy deposition by ionization is proportional to Z^2, the most important HZE ions in terms of the specific energy deposition density or specific dose density in materials are Fe ($Z = 26$) and to a lesser extent ions in the $Z = 8$–14 range.

The idea of introducing spallation processes into astrophysics arose in 1970 [28], when it was realized that abundances of some elements in the cosmic rays are significantly different than those observed in the solar system. For isotopes of Li, Be, B, F, Cl, K, Sc, Ti, V, Cr, Mn the cosmic ray abundances exceed the solar ones by at least one order of magnitude and in an extreme case of Li, Be, B – so-called LiBeB puzzle – it is even six orders of magnitude. This is seen in Figure 1.7, where the production of Li, Be, and B by high-energy spallation reactions between cosmic rays and the interstellar medium induced on C, N, and O is compared to the abundances of products of the solar system (see [15, 29–31]). The underestimation of the abundances of elements with atomic mass numbers from 20 to 25 by three to four orders of magnitude is also observed. The most possible formation of the LiBeB production is nowadays thought to be interactions of galactic comic rays with the interstellar medium, mainly carbon, nitrogen, and oxygen nuclei, where the most abundant high-energy cosmic ray particles are protons and α-particles. Other possible origins are primordial, stellar, or supernova neutrino spallation (see Refs. [32, 33]).

Stable and radioactive nuclides are produced by the interaction of solar and galactic cosmic ray particles with terrestrial and extraterrestrial matter. In extraterrestrial materials, such as meteorites and lunar surface material samples, these product nuclides are called cosmogenic nuclides. A limited number of cosmogenic nuclides is observable in the earth's atmosphere due to its relatively simple chemical composition. In extraterrestrial matter more than 30 cosmogenic nuclides have been

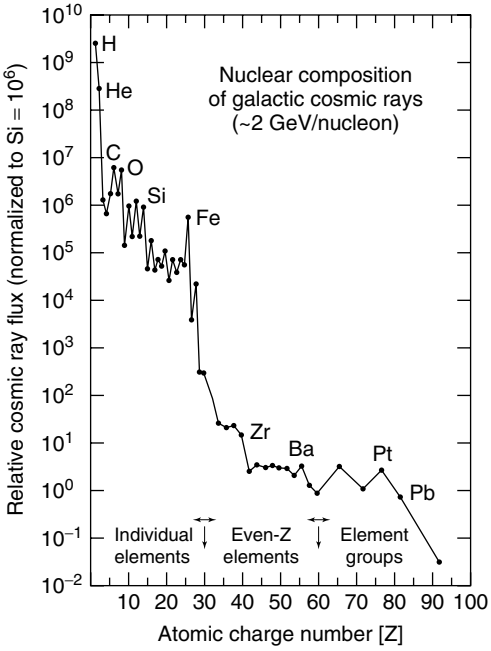

Fig. 1.6 Relative particle flux of cosmic rays as a function of the nuclear charge Z.

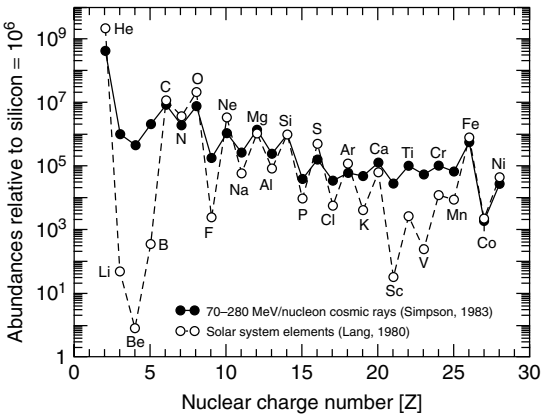

Fig. 1.7 Comparison of elemental abundances of 70–280 MeV/nucleon for cosmic rays (from Simpson [15]) and to the solar system abundances (from Cameron [29] and Lang [30]) normalized to ($Si = 10^6$).

observed. The production cross section of these nuclides with galactic cosmic or solar rays is an actual problem of modern cosmo-chemistry. To analyze the formation of the isotopic content of cosmic matter and its evolution under different radiation conditions, the knowledge of isotopic excitation functions is required. The observed

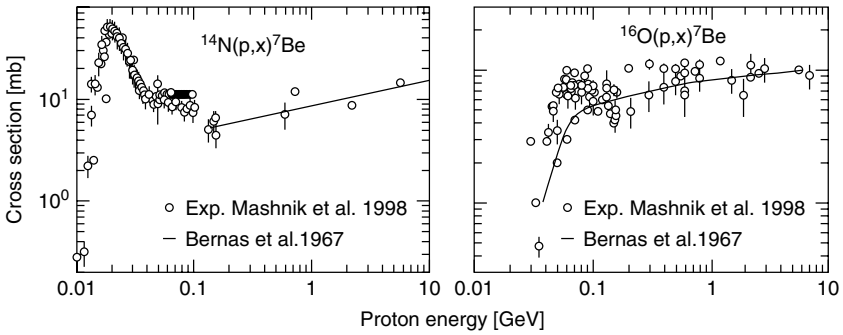

Fig. 1.8 Comparison of cross sections used in astrophysical simulations (Mashnik et al. [41] and Bernas et al. [40]).

concentrations of cosmogenic nuclides in extraterrestrial matter could be used to determine the exposure history of the irradiated specimen or the history of the cosmic radiation itself (Michel et al. [34–36]). Theoretical and experimental investigations of cosmogenic nuclides in extraterrestrial matter yield information about spectral distribution, composition, and intensity of solar and galactic cosmic rays over time scales of up to 10^9 a. By no other means than by cosmic nuclides this information about the history of the solar system may be obtained. A large number of experiments were performed in the past to demonstrate the importance of excitation functions for the production of cosmogenic nuclides (see [37–39] and also Chapter 23 on page 653). In Figure 1.8, two examples of cross sections used in astrophysical simulations (solid lines) are compared with presently available data (open circles) [40, 41].

Meanwhile, many other reliable measurements were performed [38] and compared with simulations. But experiments are unable to provide all the necessary information. Some semiempirical systematics of nuclear the spallation reaction were evaluated in the 1960s called Rudstam systematics [42]. The Rudstam systematics were than further developed by Silberberg and Tsao [43–47], taking the validity of Serber's model [2] into account. With the progress in spallation physics and the development of Monte Carlo particle reaction mechanisms and particle transport in matter during the recent years, the simulation of these reaction processes by using basic principles is possible nowadays. Experimental investigations, measurements, and validations, will be discussed and demonstrated in Part 2 on page 287.

1.3 Physics of the Spallation Process

1.3.1 Introduction

The production of secondary particles by bombarding the atomic nucleus by energetic particles was first demonstrated by Rutherford in 1919 [48], who was using α-particles on ^{14}N causing the reaction $^{14}\mathrm{N} + ^{4}\mathrm{He} \longrightarrow {}^{17}\mathrm{O} + \mathrm{p}$. In 1934 Curie and

Tab. 1.3 Examples for some neutron-producing mechanisms.

Nuclear process	Technical application	Neutron-production yield	Energy deposition (MeV/n)
400 keV D on T absorbed in titanium	D, T solid target	4×10^{-5} (n/d)	10.000
35 MeV D on liquid Li	Deuteron stripping	3×10^{-3} (n/d)	10.000
100 MeV e^- on ^{238}U	Electron bremsstrahlung	5×10^{-2} (n/e)	2000
^{235}U(n,f)	Thermal fission	3 (n/fission)	190
1000 MeV protons on thick Hg target	spallation	30 (n/proton)	55
Laser-ion beam imploded pellet	(D, T) CTR fusion	1 (n/fusion)	3

Joliot [49] produced the first artificial radioactivity using α-particles by the reaction $^{27}Al + ^4He \longrightarrow ^{30}P + n$. In 1932, the invention of the cyclotron by Lawrence and Livingston [50] and in 1939 the discovery of the nuclear fission by Hahn and Strassmann [51, 52] opened new possibilities for secondary particle production as high-intensity neutrons, radioactive isotopes, gammas, pions, and muons. In addition to fission, nuclear fusion of light elements produces secondary particles such as neutrons, produces energy, and radioactive species. The fusion of light nuclei (hydrogen isotopes) was first observed by Oliphant in 1933 [53]. The cycle of nuclear fusion in stars and the subsequent reactions were worked out by von Weizsäcker [54] and Bethe [55] in 1935/1939. Candidates for terrestrial reactions for neutron production are $D + T \longrightarrow {}^4He + n + 17.59$ MeV and $D + D \longrightarrow {}^3He + n + 3.27$ MeV or in the abbreviated form $T(d,n)^4He$ and $D(d,n)^3He$, where the energy of the produced neutrons is 14.1 MeV and 2.45 MeV, respectively.

It may be therefore very useful to compare several of the above-mentioned methods from the standpoint of possible mechanisms of neutron production. Features of several processes are shown in Table 1.3. Each of the processes, except the last one, has been used for the production of neutrons for certain purposes. Since power density limits must be considered, the energy deposition per neutron is a very important parameter. The usefulness of different reactions depends not only on the values of the given table, but also on other factors, such as the energy and angular distribution of the neutrons, the range of the charged particle production in charged particle reactions, the availability of suitable accelerators, and critical constraints in the case of fission reactors [56, 57]. In the case of the controlled thermonuclear reaction (CTR) the feasibility has still to be demonstrated.

Together with one of the first projects to design and build a high-intensity neutron spallation source ''ING'' (Intense Neutron Generator) [58] experiments on thick targets were done to measure neutron production yields [59] and to evaluate the energy- or heat depositions. In Figure 1.9 these results for cylindrical thick targets of uranium and lead are shown.

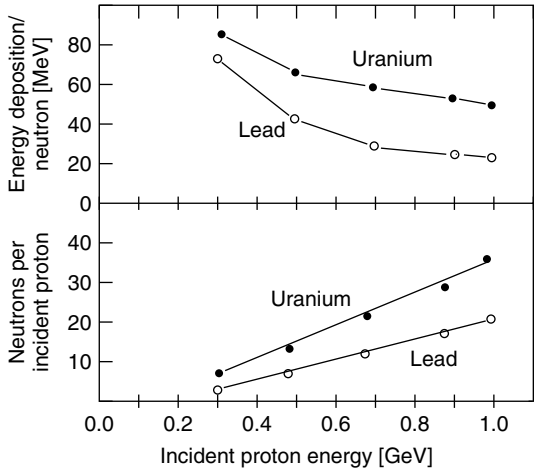

Fig. 1.9 ING measurements on neutron production yields and evaluated heat production for cylindrical targets of uranium and lead of diameter = 10 cm, and length = 60 cm.

At an incident proton energy of 1 GeV the ratio of the neutron yields and the ratio of the heat per neutron for the targets of lead and uranium (diameter = 10 cm, length = 60 cm) are

- $\text{yield}_{\text{uranium}}/\text{yield}_{\text{lead}} = 36.9/20.8 = 1.77$,
- $\text{heat}_{\text{uranium}}/\text{heat}_{\text{lead}} = 50.1/25.7 = 1.95$.

A part of the higher neutron yield for uranium comes from the ''extra''-neutrons-produced fast fission processes in uranium. The increase in heat production per neutron for the uranium target is due to fast fission. For a proton beam power of 1 MW at 1 GeV incident proton energy, the neutron source strength and the heat deposition for these targets are given in Table 1.4. For a neutron source strength of about 10^{17} neutrons per second and a proton beam power of 1 MW, a lead target would produce about 0.33 MW and a uranium target 1.2 MW.

Carpenter [56] used the measurements of Figure 1.9 to determine a semiempirical relation for the neutron yield $\gamma(E)$ production for incident proton beam energies 0.2 GeV $\leq E \leq$ 1.5 GeV as follows:

$$\gamma(E) = 0.1(A + 20)(E_{\text{GeV}} - 0.12) \quad \text{for} \quad 9 \leq A \leq^{238} \text{U}, \tag{1.4}$$

and

$$\gamma(E) = 50(E_{\text{GeV}} - 0.12) \quad \text{for} \quad ^{238}\text{U}, \tag{1.5}$$

where A is the atomic weight (g/mole) and E_{GeV} is the incident proton energy in GeV.

These semiempirical formulas (1.4) and (1.5) are only valid for targets of diameter 10 cm and length 60 cm. Other target geometries and material compositions will

Tab. 1.4 Estimated source strength and energy deposition of ''ING'' targets of Figure 1.9 on the facing page.

	Lead target	Uranium target
Source strength[a]		
Number of neutrons	1.3×10^{17}	2.3×10^{17}
Energy deposition		
(MeV)	3.3×10^{18}	1.2×10^{19}
(MW)	0.33	1.2

[a] Calculated for an incident proton beam energy of 1 GeV and 1 MW beam power = 1 GeV mA, where $1\,\text{mA} \equiv 6.24 \times 10^{15}$ protons/s and $1\,\text{W} \equiv 1\,\text{J/s}$, and $1\,\text{eV} \equiv 1.6 \times 10^{-19}$ J.

produce different neutron yields, which will arise from secondary processes such as production or absorption, of particle leakage and may be dependent on the full development of the so-called hadronic cascade inside the target.

1.3.2 The Fission Process

Because fission is a well-known process in physics and technology, it may be interesting to discuss some similarities and different basic features between spallation and fission. In the case of fission, slow neutrons of thermal energy ($E_n \approx 0.024$ eV), interact with metastable ^{235}U. The excited nucleus decays in a cascade of fission products of smaller atomic weight. These fragments, or fission products, are about equal to half the original mass. This so-called binary splitting of an excited nucleus into two approximately equal parts is still considered as one of the most interesting phenomena of collective motion of nuclear matter and as an excellent example of the nuclear multiparticle problem. According to the ''liquid drop model'' [60], regarding the nucleus as an incompressible liquid, a surface tension is responsible for the inner forces on all surface nucleons, which in turn makes the nucleus unstable against deformation. The nucleus breaks apart when the Coulomb repulsion between the two halves of the deformed nucleus equals the restoring force of the nuclear surface tension. Neutrons will occasionally be freed during the scission process, but are mainly released by evaporation from the fission fragments. The fragments are neutron rich and have an excess of internal energy. Details may seen in Refs. [61] and [62]. On average about 2.5 neutrons are produced by the fission of one ^{235}U nucleus. The sum of the masses of these fission fragments is less than the original mass. This ''missing'' mass (about 0.1% of the original mass) is converted into energy according to Einstein's equation $E = mc^2$. The so-called produced fission neutrons possess very elevated energies of about 2 MeV and are thus unsuitable for inducing further fission processes. With the help of moderators

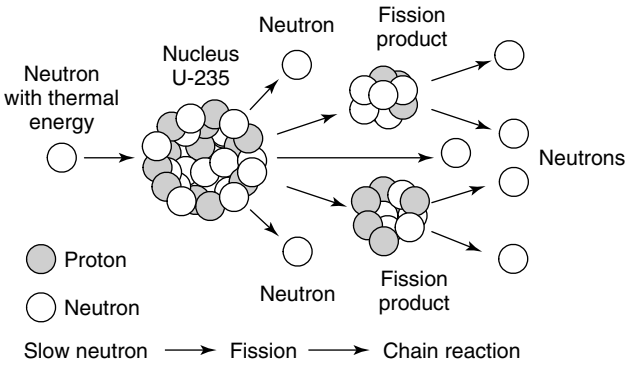

Fig. 1.10 Schematics of fission processes.

the fast neutrons are slowed down to meV energies. These slow neutrons sustain the chain reaction in a nuclear reactor. A chain reaction refers to a process in which neutrons released in fission produce an additional fission in at least one further nucleus. This nucleus in turn again produces neutrons, and the process repeats. If each neutron releases two more neutrons, then the number of fissions doubles each generation. In that case, in 10 generations there are about 1024 fissions and in 80 generations about 6×10^{23} fissions, which is a mole of fissions. In Figure 1.10, the schematic of the fission process is shown. One should refer to Sections 1.3.3, 3.4.5, 3.7, and 3.7.1 for more details of fission and spallation and fission.

The spectrum of neutrons obtained in a reactor has a broad energy distribution, reaching from 0.001 eV to over 10 MeV. It is characterized by the spectrum $\Phi(E)$. $\Phi(E)dE$ is the flux of neutrons between E and $E + dE$. Within this spectrum three different regions are distinguished:

- $E > 0.5$ MeV – the region of fast neutrons. Here $\Phi(E)$ (formula (1.6)) approximately follows the energy distribution of the neutrons produced in fission. The fission spectrum can be approximated by formula (1.7) (details may be seen also in Refs. [61, 63]) and is shown in Figure 1.11.
- 0.2 eV < E < 0.5 MeV – the region of epithermal or resonance neutrons (formula (1.8)). In this energy range, the spectrum is mainly predominated by neutrons being slowed down by elastic collisions with the nuclei of the moderator substance.
- $E < 0.2$ eV – the region of thermal neutrons. Thermal neutrons are nearly in thermodynamic equilibrium with the thermal motion of the moderator atoms. Their energy distribution can frequently be approximated by a Maxwell distribution (formula (1.9)).

$$\Phi_f = \int_{0.5\,\mathrm{MeV}}^{\infty} \Phi(E)dE \qquad (E > 0.5\,\mathrm{MeV}) \tag{1.6}$$

$$n(E) = 0.484 \cdot e^{-E} \cdot \sinh\sqrt{2E} \quad (\mathrm{MeV}) \tag{1.7}$$

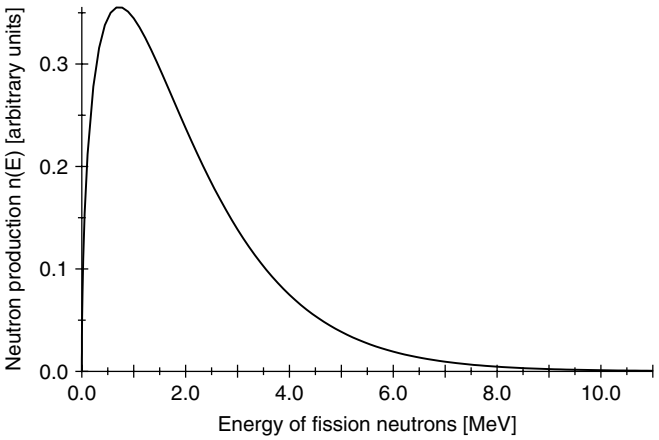

Fig. 1.11 The energy spectrum of neutrons produced in thermal neutron fission of ^{235}U using formula (1.7).

$$\Phi(E)dE = \frac{\Phi_{\text{epi}}}{E}dE \qquad (0.2\,\text{eV} < E < 0.5\,\text{MeV}) \tag{1.8}$$

$$\Phi(E)dE = \Phi_{\text{th}} \cdot \frac{E}{kT} \cdot e^{-E/kT} \cdot \frac{dE}{kT} \qquad (E < 0.2\ \text{eV}). \tag{1.9}$$

Here T is the absolute temperature and k is the Boltzmann constant, which is in fact a conversion factor between energy and temperature units. In terms of eV energy units it has a value of 8.617×10^{-5} (eV/K) with $k = 1.38 \times 10^{-23}$ (J/K) and $1\ \text{J} \simeq 6.25 \times 10^{18}$ (eV).

The spectrum of fission neutrons could also be evaluated fairly well using the Maxwell distribution in the following form:

$$n(E) = \frac{2 \cdot E^{1/2}}{\pi^{1/2} \cdot E_T^{3/2}} \cdot e^{-E/E_T}. \tag{1.10}$$

Here E_T is the kinetic energy and kT is corresponding to a certain "temperature" of the nucleons in the nucleus. Values for E_T are 1.29 MeV for ^{235}U fission and 1.33 MeV for ^{239}Pu fission corresponding to temperatures of about 1.14×10^8 K and 1.18×10^8 K, respectively. The mean kinetic energy of the neutron distribution is $\overline{E} = (3/2) \times E_T$ here.

The distribution of the energy released to the reaction products in nuclear fission is summarized in Table 1.5.

1.3.3 Spallation and Fission

In contrast to fission, the spallation process is not an exothermal process – energetic particles are necessary to enable the process. As mentioned in Section 1.1, spallation refers to nuclear nonelastic or inelastic reactions that occur when energetic

Tab. 1.5 Energy release of reaction products in nuclear fission. The fission reaction is therefore an exothermal process.

Reaction product	Released energy (MeV)
Fission fragments	167 ± 5
Neutrons	5
Prompt γ's	6 ± 1
β-particles	8 ± 1.5
Decay γ's	6 ± 1
Neutrinos	12 ± 2.5
Sum	204

subatomic particles – protons, deuterons, neutrons, pions, muons, etc. – interact with an atomic nucleus, which is usually referred to as ''target'' nucleus. In this context, energetic means kinetic energies of the primary incident particles on the target nucleus larger than several tens of MeV and more accurately, within the meaning of the validity of theoretical physical models, an incident energy of about 100–150 MeV. At these energies the deBroglie wavelength λ [64–66], e.g., of the proton, is only $\approx 10^{-13}$ cm (see Eq. (1.11)):

$$\lambda = h/\sqrt{2 \cdot m_p \cdot E_p}\,(\text{cm}) = (h \cdot c)/\sqrt{2 \cdot m_p \cdot c^2 \cdot E_p})\,(\text{cm}) \tag{1.11}$$

with $m_p = 938.2$ (MeV/c^2) the rest mass of the proton, E_p the energy of the proton in MeV, $h = 6.626 \times 10^{-34}$(J s) $= 4.136 \times 10^{-21}$ (MeV s) the Planck constant, and $h \cdot c \approx 1240 \times 10^{-7}$(eV cm).

- For proton energies $E_p = 100-150$ MeV, λ is about $\lambda \approx 2.8 \times 10^{-13}$–$2.3 \times 10^{-13}$ (cm), which is smaller as the size of the nucleus with about $\approx 10^{-12}$ (cm).
- At an incident energy of $E_p = 1000$ MeV, λ is about $\lambda \approx 9.0 \times 10^{-14}$ (cm).
- For lower incident energies, e.g., $E_p = 10$ MeV, λ is $\approx 10^{-12}$ (cm), which is the size of the nucleus. In this case a nucleon does not interact with individual nucleons, but with the whole nucleus.

At 100–150 MeV, the deBroglie wavelength λ is therefore short enough to allow the incident particle to interact with the individual nucleons inside the nucleus. As is discussed in more detail in Chapter 2, this is an important prerequisite for the application of particle nucleus collision models limiting their validity above some tens of MeV. Therefore, it is no longer correct that a spallation reaction is proceeding in the formation of a compound nucleus. The initial collision between the incident particle and the target nucleus leads to a series of direct reactions – the so-called intranuclear cascade – where individual nucleons or small groups of nucleons are ejected from the nucleus. Above a few GeV per incident nucleon fragmentation of the target nucleus may also occur. After the ''intranuclear cascade'' phase of

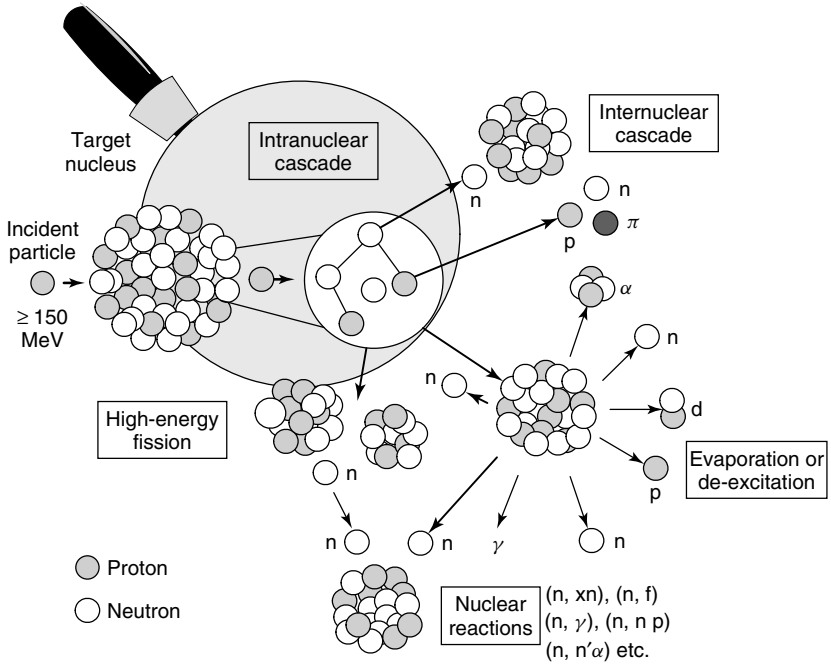

Fig. 1.12 The principal scheme of spallation.

the reaction the nucleus is left in an excited state. This is shown in principle in Figure 1.12.

During the first stage – cascade/pre-equilibrium stage – the incident particle undergoes a series of direct reactions with the nucleons–neutrons and protons – inside the target nucleus, where high-energy secondary particles such as protons, neutrons, and pions from 20 MeV up to the energy of the incident particle are created in an *intranuclear cascade* inside the nucleus. From the *intranuclear cascade* some of these high-energy hadrons escape as secondary particles. Also low-energy pre-equilibrium particles in the low MeV energy range are ejected from the nucleus leaving the nucleus in a highly excited state. In the second stage nuclear de-excitation or *evaporation* takes place, when the excited nucleus relaxes by emitting low-energy (<20 MeV) neutrons, protons, alpha particles, light heavy ions, residuals, etc., with the majority of the particles being neutrons. After evaporation the nucleus that remains may be radioactive and may emit gamma rays.

The secondary high-energy particles produced during the *intranuclear cascade* phase move roughly in the same direction as that of the incident particle beam, due to the so-called Lorentz boost, e.g., the momentum transfer of the incident particle, and can collide with other nuclei in the target. The reactions that follow are a series of secondary spallation reactions (see Figure 1.12) that generate more secondary particles and low-energy neutrons. This so-called *internuclear cascade* or more general *hadronic cascade* is the accumulation of all reactions caused by primary and secondary particles in a target.

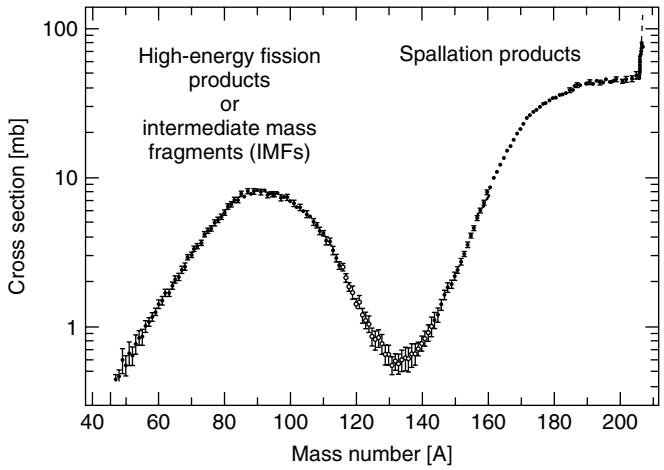

Fig. 1.13 Experimentally measured spallation residual mass distributions from [68] of 1 A GeV ^{208}Pb + p reactions.

For some target materials, low-energy spallation neutrons (<20 MeV), e.g., pre-equilibrium/evaporation neutrons, may enhance the neutron production through low energy (n,nx) reactions. For very heavy nuclei, e.g., lead, tungsten, thorium, and natural or depleted uranium, the so-called *high-energy fission* can occur during the *evaporation phase* in competing with standard *evaporation*. Details are given in Chapter 3. Thorium and uranium are, in addition to undergoing high-energy fission, fissionable by low-energy (1–20 MeV) neutrons.

Fission and spallation differ in several ways [67]. One important difference is in the nuclear debris remained after the reaction is completed. In spallation, the nuclei that remain after evaporation are about 15 atomic mass units lighter, on average, than the original target nucleus, because very light particles such as protons and neutrons are emitted. In spallation, the nuclear debris – sometimes called *spallation residuals* – is distributed close to the original target material. A typical distribution measured for protons of 1 GeV on a ^{208}Pb target is illustrated in Figure 1.13. Note that *high-energy fission* produces symmetric fission products or intermediate mass fragments peaking in a range around an atomic mass $A = 90$.

In fission, the nucleus divides into two fragments (Figure 1.10), typically producing a light fragment and a heavy fragment as fission products. For high-energy fission, the fission product distribution is more symmetric than the asymmetric fission products caused by low-energy neutrons. This is because at high energy – beyond some MeV – any shell effects are washed out. Another difference is in the number of neutrons released (Table 1.3). The overall number of neutrons released per fission event of about 2.5 to 3.0 is considerably less than that released per spallation event with about 25 to 30 using heavy target materials bombarded by 1 GeV energy protons.

The amount of energy deposited per neutron produced in spallation and fission (Table 1.3) is also different. For fission, about 200 MeV of energy is deposited as

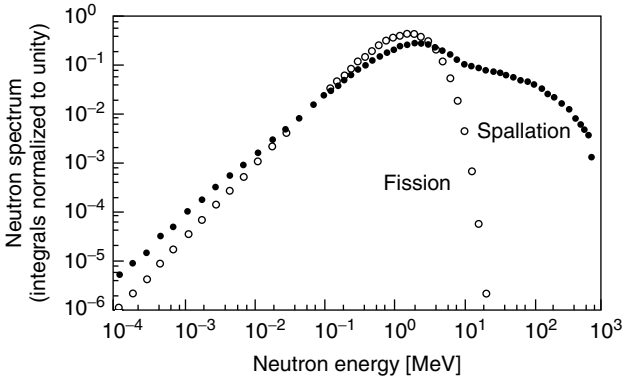

Fig. 1.14 Spallation neutron spectrum compared to a typical neutron spectrum from thermal neutron fission of ^{235}U. The spallation spectrum is measured at 90° from a "finite" 10 cm diameter by 30 cm long tungsten target bombarded by 800 MeV protons [67].

heat for each neutron produced; for spallation in Hg, the corresponding number is about 55 MeV. Although there is less heat generated with spallation, the beam power intensity of a proton beam of a high power spallation source can lead to cooling problems in target systems (cf. Part 3 on page 495). Spallation neutrons have higher energies than fission neutrons (cf. Figure 1.14). In a spallation source high-energy cascade neutrons approach the energy of the incident proton beam energy [67]. The high-energy tail of the spallation neutron spectrum compared to the fission spectrum is remarkable. High-energy neutrons are extremely penetrating. Therefore, well-designed shielding is needed to prevent high-energy neutrons from causing unwanted problems in radiation safety (cf. Chapter 7 on page 233).

1.3.4
The Logical Scheme of Spallation Reactions

The low-energy (<20 MeV) cascade, evaporation, and fission neutrons are isotropic in angle, whereas the high-energy (>20 MeV) neutrons from spallation have a strong angular dependence, where, in the very forward direction, these neutrons can have the same energy as the incident particle beam causing the spallation event. This is shown in Section 1.3.7.6. Also some of the features of the most important atomic interactions such as ionization, excitation effects and Coulomb scattering and hadron, pion, and muon decay will be discussed in Section 1.3.5 to complete the physics of spallation. In Figure 1.15, a logical scheme of performance of the spallation process is shown.

In spallation a certain fraction of the incoming particle's energy is transferred to the nucleus by nucleon–nucleon collisions, thus increasing the kinetic energy of the nucleons inside the nucleus, or, more precise heating up the nucleus. Three stages can be distinguished in a spallation reaction according to a certain time

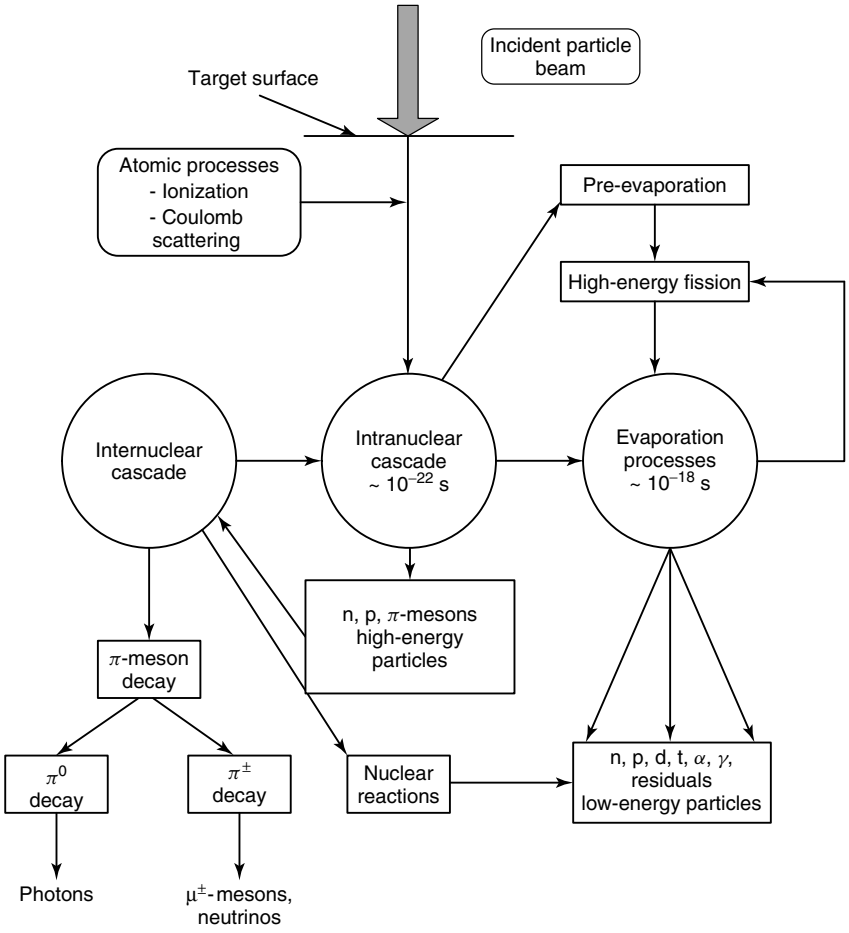

Fig. 1.15 A logical scheme of the performance of spallation reactions showing the three stages on particle production.

scale, the *intranuclear cascade phase*, the *pre-equilibrium phase*, and the *evaporation and high-energy fission phase*. This is schematically shown in Figures 1.12 and 1.15.

In the initial *cascade*, so-called *intranuclear cascade*, which takes place within about 10^{-22} s, the energy of the primary incident particle is transferred to the nucleons inside the target nucleus. During this process energetic particles may leave the nucleus and may induce another spallation reaction in a different nucleus – *internuclear cascade*. *Internuclear cascade* processes are generated in thick targets. This processes are called particle showers that means a cascade of secondary particles produced in interactions of high-energy particles in dense matter. As mentioned earlier, the *intranuclear cascade* is often called *hadron cascade* because during this phase charged pions, neutrons, and protons are produced. After the completion of the *intranuclear cascade*, the kinetic energy possessed by those nucleons which remain inside the nucleus is assumed to be equilibrated

among all of the nucleons. This residual excitation energy, as well as the mass and charge of the residual nucleus, can take a range of values because of the variety of different outcomes, e.g., neutrons, protons, pions, etc., possible for the reactions at high energies. Subsequent de-excitation is determined by the so-called *evaporation*, which occurs within a time frame of about 10^{-18} s or less. Thus, the second stage of a spallation reaction is the *evaporation phase*, which may compete with the so-called *high-energy fission* when using heavy target nuclei. Particles emitted during the *evaporation phase* are of low energies (1–10 MeV) and have isotropic angular distributions. Nucleon emission, especially of neutrons, in particular for targets with high atomic masses, is more probable than the emission of positively charged clusters such as deuterons, tritons, ^{3}He, or α or even heavier particles. After particle emission is no longer energetically possible, the nucleus can still be left with a small amount of excitation energy, which is assumed to be released by photon emission.

1.3.5 Particle Interaction Mechanisms

This section gives a brief review about the basic forces, the classification of the fundamental particles, and some useful definitions concerning particle interaction with matter and transport in matter. When energetic particles with energies above several tens of MeV undergo *nuclear interactions* with matter they will produce either charged secondary particles, e.g., protons, tritons, deuterons, α-particles, light and heavy ions, π-mesons, electrons and positrons or uncharged neutrons, and photons. Electrons, positrons and photons can undergo further interactions with matter inducing an *electromagnetic cascade*.

In principle, there are seven types of particles of concern to spallation reactions and their application:

- protons and charged heavier particles of masses comparable to the mass of protons, tritons, deuterons, α-particles, etc.,
- neutrons at high energies – from some tens of MeV to several GeV,
- electrons and positrons,
- photons and γ-radiation,
- π-mesons and their decay products, μ-mesons
- also antiparticles such as the antiproton $\overline{p}$ or the positron e^+ may be used to invoke spallation reactions,
- neutrons at low energies – from meV to some tens of MeV.

1.3.5.1 The Elementary Forces and Particles

The present knowledge of the physical phenomena suggests that there are four types of forces between physical bodies (Table 1.6). These forces are of decreasing strength, from the strong to the electromagnetic, the weak and the gravitational. The strong, the electromagnetic, and the weak forces determine the properties of the interactions on nucleon–nucleon or nucleon–nucleus collisions in the spallation process.

The *standard model* in particle physics describes the known elementary particles and their interactions. According to the *standard model* there are six quarks and

Tab. 1.6 Elementary particles and forces.

Force	Strong	Electromagnetic	Weak	Gravitational
Particles experiencing	**Quarks, gluons**	**Electrically charged**	**Quarks, leptons**	**All**
Particles mediating	Gluons	Photons	Bosons W^+, W^-, Z^0	Graviton?
Strength at 10^{-13} cm compared to the strong force	1	10^{-2}	10^{-13}	10^{-38}
Range (cm)	$\leq 10^{-13}$	∞	$\leq 10^{-16}$	∞
Approx. mass (GeV/cm^2)	0	0	80.4, 80.4, 91.2	0
Electric charge	0	0	$+1, -1, 0$	0
Spin	1	1	1, 1, 1	2

each of them has three different *colors*. The *neutron* and the *proton*, and many other particles heavier than the proton and the neutron, the *baryons*, are made of three quarks and the *mesons* are made of a *quark* and an *antiquark*. The inner structure of such objects has been studied, for example, with high-energy electrons and it has been found that at higher bombarding energies – several GeV – additional quark–antiquark pairs are being ''resolved" and a part of the energy and the momentum of these particles is not carried by the quarks, but by the massless gluons mediating the strong force. The simple picture of a proton or neutron composed only of three valence quarks has therefore to be extended to a more complex structure still not exactly understood. Other particles, such as the *electron* and the *muon* and the *neutrinos* are *leptons* and do not seem to have an internal structure. So the fundamental scheme of subatomic particles leads to the existence of *12 elementary* particles. Their properties are given in Tables 1.7, 1.8, and 1.10. More details about the particle properties and the standard model are given in the references of the PDG [19] and in Refs. [69–71]. Quarks and leptons are the elementary particles which build up matter. The *quarks* are the ''bricks'' for all known *mesons* and *baryons*. More than 200 mesons and baryons are known.

Gluons are the exchange particles for the so-called *color force* between *quarks*, analogous to the exchange of *photons* in the *electromagnetic force* between two charged particles. The gluon can be considered to be the fundamental exchange particle for the strong interaction between protons and neutrons in a nucleus. The short-range *nucleon–nucleon* interaction can be considered to be a *residual color force* extending outside the boundary of the proton or neutron. The strong interaction is involved by the exchange of pions, and indeed the theory of the Yukawa potential

Tab. 1.7 Properties of the leptons (the charge is given in terms of the elementary charge of the electron $e = 1.602 \times 10^{-19}$ (*C*)).

Particle name	Symbol	Approx. mass (GeV/c^2)	Electric charge	Mean life (s)	Spin ($\hbar$)
Electron neutrino	ν_e	$<1.0 \times 10^{-8}$	0	Stable	1/2
Electron	e^+ or e^-	0.000511	−1	Stable	1/2
Muon neutrino	ν_μ	<0.0002	0	Stable	1/2
muon	μ^+ or μ^-	0.106	−1	2.197×10^{-6}	1/2
Tau neutrino	ν_τ	<0.02	0	Stable	1/2
Tau	τ^+ or τ^-	1.7771	−1	2.91×10^{-13}	1/2

Tab. 1.8 Properties of the quarks.[a]

Particle name	Symbol	Approx. mass (GeV/c^2)	Electric charge	Spin ($\hbar$)
Up	u	0.0015 − 0.003	+2/3	1/2
Down	d	0.003 − 0.007	−1/3	1/2
Charm	c	1.25	+2/3	1/2
Strange	s	0.095	−1/3	1/2
Top	t	174.2	+2/3	1/2
Bottom	b	4.2	−1/3	1/2

[a] The masses should not be taken too seriously, because the confinement of the quarks implies that one can not isolate them to measure their masses directly. They are only determined by scattering experiments.

of Yukawa in 1935 [72] was helpful in developing our understanding of the strong force. Some features of the pions are summarized in Table 1.11.

The quarks are *fermions* and possess the quantum numbers as given in Table 1.9.

Baryons are massive particles which are made up of three quarks in the standard model (see Table 1.10). This class includes the proton and the neutron. There are others such as lambda, sigma, etc. Baryons are different from *mesons* in that mesons are composed of only two quarks. Baryons and mesons are included in the class known as *hadrons*, the particles which interact by the strong force (Table 1.6). This general classification excludes *leptons*, which do not interact by the strong force. But the weak interaction acts on both *hadrons* and *leptons*. Hadrons as seen in Table 1.10 are composed of quarks, either as quark–antiquark pairs (mesons) or of three quarks (baryons).

Tab. 1.9 The quantum numbers of the quarks.

Type	Down	Up	Strange	Charm	Bottom	Top
Symbol	d	u	s	c	b	t
Spin	1/2	1/2	1/2	1/2	1/2	1/2
Charge	−1/3	2/3	−1/3	2/3	−1/3	2/3
Isospin (T)	1/2	1/2	0	0	0	0
T_3	−1/2	1/2	0	0	0	0
Strangeness	0	0	−1	0	0	0
Charm	0	0	0	1	0	0
Bottom	0	0	0	0	−1	0
Topness	0	0	0	0	0	1
Baryon number	1/3	1/3	1/3	1/3	1/3	1/3

Tab. 1.10 Properties of the baryons.

Particle name	Symbol	Quark makeup	Approx. mass (MeV/c^2)	Electric charge	Spin($\hbar$)	Mean life (s)	Dominant decay modes
Proton	p	uud	938.3	+1	1/2	Stable	$\cdots$
Neutron	n	ddu	939.6	0	1/2	920	$pe^-\overline{\nu}_e$
Lambda	Λ^0	uds	1115.6	0	1/2	2.6×10^{-10}	$p\pi^-, n\pi^0$
Sigma	Σ^+	uus	1189.4	+1, −1	1/2	0.8×10^{-10}	$p\pi^0, n\pi^+$
	Σ^-	dds	1197.3			1.5×10^{-10}	$n\pi^-$
	Σ^0	uds	1192.5	0	1/2	6.0×10^{-20}	$\Lambda^0\gamma$
Delta	Δ^{++}, Δ^0	uuu, udd	1232	+2, 0	3/2	0.6×10^{-23}	$p\pi^+/n\pi^0, p\pi^-$
	$\Delta^{\pm}$	uud, ddd	1232	+1, −1	3/2	0.6×10^{-23}	$p\pi^0, n\pi^+/n\pi^-$

1.3.5.2 Feynman Diagrams

Feynman diagrams are the graphical way to represent the exchange of particle forces [73, 74]. Each point at which lines come together is called a vertex, and at each vertex one may examine the conservation laws which govern particle interactions. Each vertex must conserve charge, baryon, and lepton number. Particles are represented by lines with arrows to denote the direction of their travel, with antiparticles having their arrows reversed. Virtual particles are represented by wavy or broken lines and have no arrows.

Figure 1.16 shows examples of Feynman diagrams for the three forces, the electromagnetic, the weak, and the strong interactions between quarks and between nucleons. Particle interactions can be represented by these diagrams with at least two vertices. They can be drawn for protons, neutrons, etc., even though they are composite objects and the interaction can be visualized as being between their constituent quarks.

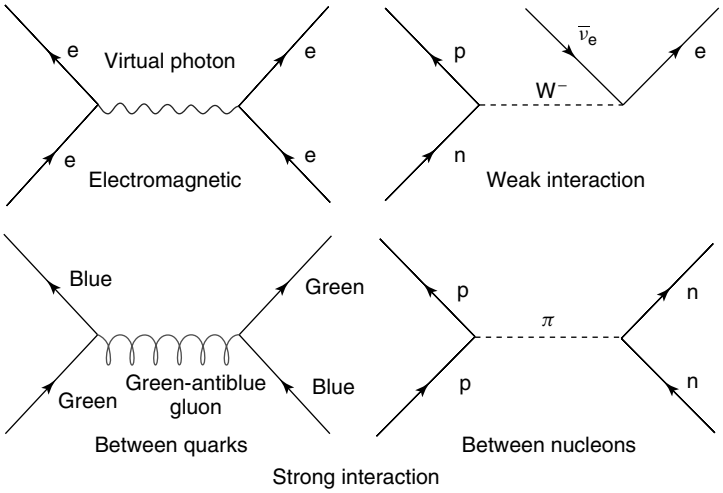

Fig. 1.16 Examples of particle interactions, electromagnetic, weak, and strong interactions between quarks and between nucleons represented by Feynman diagrams.

1.3.5.3 Resonance Decay, Pion Absorption, and Pion Charge-Exchange

Resonance decay Heisenberg suggested in 1932 that the proton and neutron could be treated as different substates of one particle, the nucleon. A nucleon is ascribed a quantum number, isospin I, with a value $I = 1/2$ with two substates $I_1 = +1/2$ for the proton, and $I_2 = -1/2$ for the neutron. The quark model explains in a simple way the conservation laws of the quantum numbers (see Table 1.9) in strong interaction between hadrons or between pions and hadrons. Baryons and mesons are composed of multiplets of members with different charges, but approximately of the same mass. Examples of these are the triplets of π^+, π^-, and π^0, the doublet of nucleons and the quartet of Δ's. This can be represented by attributing to the members of each multiplet the same isotopic spin or isospin T, which is related to the multiplicity M of the members of the multiplet by $M = 2T + 1$ and a different third component T_3. The number of members of hadron multiplets is limited to the maximum number of four so the isotopic spin of a hadron cannot exceed 3/2. It should be noted that to the highest charge member of each multiplet the highest value of T_3 is attributed and to the lowest charge member the lowest. Thus in the Δ-quartet made up of Δ^{++}, Δ^+, Δ^0, and Δ^-, the sequence of the isospin values of T_3 is 3/2, 1/2, $-1/2$, and $-3/2$, respectively. More details could be see in Refs. [70, 75].

The early theoretical studies and investigations by Sternheimer–Lindenbaum [76] on secondary particle production in nucleon–nucleon or pion–nucleon interactions were concentrated on the question which spin and isospin contribute to the production process. The Sternheimer–Lindenbaum model assumes that one or more *isobars* [76] or nowadays called *resonances* are produced in such collisions. A number of intranuclear cascade models utilize the Sternheimer–Lindenbaum isobar model such as those of Bertini [12, 77] (see e.g., Section 2.2.3.1), Barashenkov

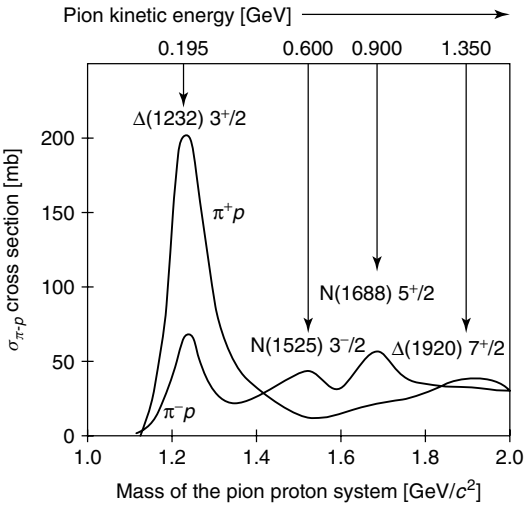

Fig. 1.17 Resonant structure of cross sections for the interaction of π^+ and π^- with protons.

et al. [10, 78], and Harp [79]. Secondary particles produced in nucleon–nucleon and pion–nucleon collisions are observed as Δ- or N-resonances (see Figure 1.17) in the cross sections of a given reaction. Complete tables of the baryon resonances, their masses, decay, spin, isospin, and quark makeup are given in the review of particle physics of the PDG reference Yao et al. [19]. Many of these particles have such a long lifetime on the *subnuclear* time scale (see Tables 1.7, 1.10, and 1.11) that it is possible to produce intense secondary beams such as pion and kaon beams of meson factories.

In Figure 1.17, the lower pion mass resonances correspond to the doubly charged Δ^{++} and neutral Δ^0 members of a quartet of particles (see Table 1.10) called the Δ_{33}- or the (3, 3)-resonance with a mass of 1232 MeV/c^2, a spin and parity of $J^p = 3/2^+$, and an isospin of $I = 3/2$. As Figure 1.17 indicates, more pion–nucleon resonances are observed, for example, there is an $I = 1/2$ resonance at 1525 MeV. The symbol Δ refers here to resonances of $I = 3/2$ and N refers to $I = 1/2$. The positions of some other known states together with their spin-parity assignments are given. Higher mass resonances are also shown. Figure 1.18 shows the resonance decay of the $\Delta(1232)^{++}$ mass in π^+ and proton as a Feynman diagram by using the quark makeup of the Δ resonance.

Pion absorption It should be mentioned that the absorption of pions by nuclei has long been of interest to nuclear physicist. The pion cannot be absorbed on a free nucleon and still conserve energy and momentum. Therefore, at least two nucleons must be involved in the absorption process. This yields even for nucleons inside a complex nucleus to make pion absorption on a nucleon in the nucleus obey energy and momentum conservation well above the Fermi momentum [80]. Several

Tab. 1.11 Properties of some important mesons.

Particle name	Symbol	Anti particle	Makeup	Rest mass (MeV/c^2)	Mean life (s)	Dominant decay modes
pion	π^+	π^-	$u\overline{d}$	139.6	2.6×10^{-8}	$\mu^+\nu_\mu$
pion	π^0	Self	$(u\overline{u} + d\overline{d})/\sqrt{2}$	135.0	0.83×10^{-16}	2γ
kaon	k^+	k^-	$u\overline{s}$	493.7	1.24×10^{-8}	$\mu^+\nu_\mu, \pi^+\pi^0$
kaon	k_s^0	k_s^0	1[a]	497.7	0.89×10^{-10}	$\pi^+\pi^-, 2\pi^0$
kaon	k_L^0	k_L^0	1[a]	497.7	5.2×10^{-8}	$\pi^+ e^- \overline{\nu}_e$
eta	η	Self	2[b]	548.8	$<10^{-18}$	$2\gamma, 3\gamma$
eta prime	η'	Self	2[b]	958	5×10^{-19}	$\pi^+\pi^-\eta$
rho	ρ^+	ρ^-	$u\overline{d}$	770	0.4×10^{-23}	$\pi^+\pi^0$
rho	ρ^0	Self	$u\overline{u}, d\overline{d}$	770	0.4×10^{-23}	$\pi^+\pi^-$
omega	ω^0	Self	$u\overline{u}, d\overline{d}$	782	0.8×10^{-22}	$\pi^+\pi^-\pi^0$
phi	φ	Self	$s\overline{s}$	1020	20×10^{-23}	$k^+k^-, k^0\overline{k}^0$

[a] The neutral kaons represent symmetric and antisymmetric mixtures of quark combinations down-antistrange and antidown-strange.
[b] The neutral eta is a quark combination $(u\overline{u} + d\overline{d} - 2s\overline{s})/\sqrt{6}$.

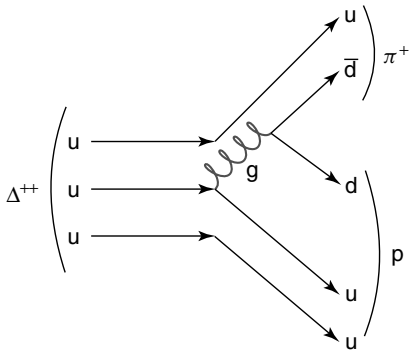

Fig. 1.18 Feynman diagram of the resonance decay of the $\Delta(1232)^{++}$ mass in π^+ and proton (g stands for the gluon exchange particle as the color force between quarks; see Section 1.3.5.1).

experiments indicted that pion absorption in nuclei in the energy region of the Δ-resonance often involved more than two nucleons, e.g., the BGO Ball experiment at LAMPF [81]. The prototype of the pion two-nucleon absorption process is the reaction $\pi^+ + d \rightarrow pp$ which is the dominant reaction on $I = 0$ pn-pairs and is sometimes referred to as the quasideuteron absorption. Contributions from the absorption, e.g., on $I = 1$ pp-pairs are much less important, especially near the peak of the Δ-resonance. A recent review is given in Ref. [80] and the experimental work contains most of the data taken at meson factories reviewed in [82].

Pion charge exchange An important example of the conversation law in particle interactions is the isospin conservation arising in the strong interaction of non-identical particles, which will generally consist of mixtures of different isospin states. An example is the pion–nucleon scattering process.

The isospin for the pion is $I_\pi = 1$ and for the nucleon $I_N = 1/2$; therefore, they may couple to $I_{\text{total}} = 1/2$ or $3/2$. If the strong interactions depend only on I and not on T_3, then 3×2 pion–nucleon scattering processes can be described in terms of two isospin amplitudes (for details see Refs. [70, 75]). Six elastic scattering processes are possible.

- Of the six elastic scattering interactions, processes

$$\pi^+ p \longrightarrow \pi^+ p, \quad \pi^- n \longrightarrow \pi^- n \tag{1.12}$$

  have $T_3 = \pm 3/2$, $I = 3/2$ and differ only in the sign of T_3.
- the cross sections

$$\pi^- p \longrightarrow \pi^- p, \quad \pi^- p \longrightarrow \pi^0 n \tag{1.13}$$

- and the cross sections

$$\pi^+ n \longrightarrow \pi^+ n, \quad \pi^+ n \longrightarrow \pi^0 p \tag{1.14}$$

  have $T_3 = \pm 1/2$, $I = 1/2$ or $3/2$.

The cross sections of Eqs. (1.12) and (1.13) are poor elastic ones, whereas the cross sections of Eqs. (1.14) are pion-exchange cross sections.

1.3.5.4 Kinetic Energy, Total Energy, and Momentum

Kinetic energies of particles are measured in units of electron volts (eV), corresponding to the kinetic energy needed by a particle of electron charge crossing a potential difference of 1 V: 1 eV = 1.602×10^{-19} J.

In particle and accelerator physics, usually the motion of energetic particles is subject to relativistic kinematics; therefore, some basic well-known properties are given below. For more details see the references in standard university textbooks such as [83, 84].

The rest energy, E_0, of a particle is defined as

$$E_0 = m_0 \cdot c^2, \tag{1.15}$$

where $m_0 =$ *particle* rest mass, $c =$ velocity of light $\equiv 2.997 \times 10^{10}$ cm s^{-1}.

The total energy, E, is given by

$$E = m \cdot c^2 = m_0 \cdot c^2 (1 - \beta^2)^{1/2}, \tag{1.16}$$

where m is observed mass of the particle, and $\beta = v/c$.

The kinetic energy, E_{kin}, of the particle is then given by

$$E_{\text{kin}} = E - E_0 = (m - m_0) \cdot c^2. \tag{1.17}$$

From Eqs. (1.15) and (1.16) it follows that

$$\beta = v/c = [1 - (E_0/E)^2]^{1/2}. \tag{1.18}$$

The momentum, p, of the particle is then

$$p = m \cdot v = m \cdot \beta \cdot c = (1/c) \cdot (E^2 - E_0^2)^{1/2} = (1/c) \cdot [E_{\text{kin}}(E_{\text{kin}} + 2E_0)]^{1/2}. \tag{1.19}$$

From Eq. (1.19) one can see that at high kinetic energies ($E_{\text{kin}} \gg 2E_0$) the particle momentum p is approximately

$$p \approx E_{\text{kin}}/c \approx E/c. \tag{1.20}$$

Equation (1.20) shows the correlation between energy and momentum frequently used by the units MeV/c or GeV/c for the particle momentum in spallation and particle research or in accelerator physics.

1.3.5.5 Cross Sections, Absorption Length, Collision Length, and Mean Free Path

The cross section is an extremely important concept in describing the interaction of particles with matter. The angular and energy distribution of particles produced in nuclear reactions with matter is usually expressed by so-called partial or double differential cross sections. The probability of producing a particle of energy E in the energy range $E + dE$ during an interaction of particles with matter in the solid angle region between Ω and $\Omega + d\Omega$ is denoted by

$$d^2\sigma/dE\, d\Omega. \tag{1.21}$$

The following basic definitions and some relations are taken from Bock and Vasilescu in [85]. The cross sections of two colliding particles is a measure of the probability that the two particles interacts. The cross section σ is a Lorentz invariant measure of the probability of interactions in a two-particle initial state. It has the dimension of an area (unit cm^2 or barn $\equiv 10^{-24}$ cm^2), and is defined such that the expected number of interactions in a small volume $d\mathbf{r}$ and a time interval dt is given as

$$dN = F \cdot \sigma \cdot d\mathbf{r}\, dt, \tag{1.22}$$

with $F = \rho_1(\mathbf{r}, t) \cdot \rho_2(\mathbf{r}, t) \cdot u$, and $u = \sqrt{(|\mathbf{u}_1 - \mathbf{u}_2|^2 - |\mathbf{u}_1 \times \mathbf{u}_2|^2)}$.

The parameters ρ_1 and ρ_2 are the number densities of the two particle species – number of particles per volume – and $\mathbf{u}_1$ and $\mathbf{u}_2$ are their velocities,

respectively. So ρ and u are the particle flux and the relative direction, respectively. The cross section may be visualized as the area presented by the target particle or by a ''thin'' *target*, which must be hit by the point-like particle for an interaction to occur. The term interaction may be specified by the final state of the reaction. As an example an elastic scattering reaction may serve. If a particle 1 is scattered into a solid angle $d\Omega$, the cross section may be denoted as $d\sigma$, and by the above definitions, the so-called *differential cross section* is given by

$$d\sigma/d\Omega = \frac{1}{F} \cdot dN/d\Omega. \tag{1.23}$$

The integration of these partial cross sections over an appropriate range of energy and in space gives the total cross section σ_{tot} often abbreviated as σ_T. The total cross section is $\sigma_T = \sigma_{\text{elastic}} + \sigma_{\text{nonelastic}}$. The cross section $\sigma_{\text{nonelastic}}$ is often named as $\sigma_{\text{inelastic}}$. For the processes of nonelastic interactions of hadrons with matter the so-called *mean free path* for absorption is important. The mean free path is therefore determined by the nonelastic part of the hadronic cross section.

The *mean free path* of a particle in matter is a measure of its probability of undergoing interactions of a given kind. It is related to the cross section corresponding to this special type of interaction.

- mean free path or interaction length:

$$\lambda_{\text{meanfp}} = A/(N_A \cdot \rho \cdot \sigma_{\text{nonelastic}}) \tag{1.24}$$

with

- σ = cross section (b) or (cm^2),
- λ_{meanfp} = mean free path or interaction length (cm),
- A = atomic weight (g/mole),
- N_A = Avogadro number(6.022×10^{23}/mole),
- ρ = target density (g/cm^3).

Tables often give $\lambda_{\text{meanfp}} \cdot \rho$ in the dimension (g/cm^2). The *collision length* λ_T often named as *nuclear collision length* and the probability density function $\Phi(x)$ as the distance between successive collisions of a particle in matter are the functions of the total cross section σ_{tot} or σ_T and are given by the following expressions:

- nuclear collision length:

$$\lambda_T = A/(\sigma_T \cdot N_A \cdot \rho) \tag{1.25}$$

- probability density function:

$$\Phi(x)dx = (1/\lambda_T) \cdot \exp(-x/\lambda_T)dx. \tag{1.26}$$

Because $\sigma_T > \sigma_{\text{nonelastic}}$ it always follows that $\lambda_T < \lambda_{\text{nonelastic}}$.

Tab. 1.12 Total and nonelastic cross sections for different media together with the nuclear collision length and the interaction length or mean free path (the values are based on Refs. [19, 86–91]).

Medium	Z	A	Density (g/cm^3)	σ_T (b)	$\sigma_{\text{nonelastic}}$ (b)	Nuclear collision length λ_T (cm)	Interaction length λ_{meanfp} (cm)
H_2	1	1.0079	0.0838	0.0387	0.033	516.7	606.21
He	2	4.0026	0.1294	0.133	0.102	385.82	503.09
Li	3	6.941	0.534	0.210	0.157	102.24	137.45
Be	4	9.0121	1.848	0.268	0.199	30.19	40.69
C	6	12.011	2.265	0.331	0.231	26.58	38.10
Al	13	26.981	2.7	0.634	0.421	26.15	39.4
Fe	26	55.845	7.87	1.120	0.703	10.52	16.76
Cu	29	63.546	8.96	1.232	0.782	9.55	15.05
W	74	183.84	19.3	2.767	1.65	5.72	9.64
Au	79	196.97	19.32	2.990	1.72	5.9	9.9
Hg	80	200.59	13.57	3.03	1.74	8.1	14.11
Pb	82	207.2	11.35	3.08	1.77	10.23	17.07
U	92	238.03	18.95	3.378	1.98	6.17	10.50
Concrete			~2.5	–	–	26.9	39.96

In Table 1.12 on the following page some values of different media for σ_T, $\sigma_{\text{nonelastic}}$, the mean free path λ_{meanfp}, and the nuclear collision length λ_T are given.

The dependence of the cross sections on incident particle energy, incident particle species, and semiempirical expressions for cross section evaluation are given in Section 1.3.7.4.

1.3.6 Electromagnetic and Atomic Interactions

The most important atomic interactions of charged particles with matter are usually ionization and excitation effects, and, occasionally, Coulomb scattering. The physics of such atomic interactions for hadrons is well known. Neutral particles such as neutrons or photons interacting with matter first produce charged particles, which then in turn produce ionization effects. Some of the basic features, which are important to understand energy deposition and the dissipation by energy losses of particles passing through matter will be given.

1.3.6.1 Energy Loss of Heavy Particles by Ionization and Excitation – the Bethe or Bethe–Bloch Formula

Charged particles lose their kinetic energy passing through matter by excitation of bound electrons and ionization. Excitation processes such as $e^- + \text{atom} \rightarrow \text{atom}^* + e^- \rightarrow \text{atom} + \gamma$ produce low-energy photons. More important are direct

collision processes where "heavy" charged particles other than electrons or photons lose energy primarily by ionization and atomic excitation. This energy loss is important for hadrons because the mean free path and the nuclear collision length for the strong interactions are large (see Table 1.12). The mean energy loss of heavy charged particles, the so-called *stopping power dE/dx* is given by the Bethe formula [92, 93] often named as Bethe–Bloch formula [19, 94–97]:

$$-\frac{dE}{dx} = 4\pi \cdot N_A \cdot r_e^2 \cdot m_e \cdot c^2 \cdot z^2 \cdot (Z/A)(1/\beta^2) \times \left[\ln\left(\frac{2m_e \cdot c^2 \cdot \gamma^2 \cdot \beta^2}{I}\right) - \beta^2 - \delta/2\right], \tag{1.27}$$

where the parameters are as follows:

- N_A – Avogadro number (6.02×10^{23} mol^{-1})
- r_e – classical electron radius (2.82×10^{-13}cm)
- m_e – electron rest mass (0.511 MeV/c^2)
- z – projectile charge in units of the elementary charge
- Z – atomic number
- A – atomic weight of the medium (g/mole)
- γ – Lorentz factor ($=\frac{E}{m_0 \cdot c^2}$), where m_0 is the rest mass (for example for a muon with $m_\mu c^2 = 106$ MeV and energy $E = 1.06$ GeV the Lorentz factor is $\gamma = 10$)
- β – projectile velocity in units of $c(=v/c)$
- I – average ionization potential of a medium, which may be approximated by $I = 16 \cdot Z^{0.9}$ eV for $Z > 1$. I is also a function of the molecular binding of the atoms of the medium. I=15 eV for atomic hydrogen, 19.2 eV for molecular hydrogen, and 21.8 eV for liquid hydrogen.
- δ – density correction, which takes into account shielding effects by the electrons of the medium on the transversal electrical field of the incident relativistic charged particles. The density correction therefore reduces the energy loss of charged particles incident on high density media such as iron or lead.

A useful abbreviation is the constant

$$4\pi \cdot N_A \cdot r_e^2 \cdot m_e \cdot c^2 = 0.3071 \frac{\text{MeV}}{\text{g/cm}^2} \tag{1.28}$$

and an approximation by using the maximum kinetic energy $E_{\max}$, which can be imparted to a free electron in a single collision leads to an abbreviated form of the Bethe–Bloch formula as given by Eq. (1.31):

$$E_{\max} = 2 \cdot m_e \cdot c^2 \cdot z^2 \cdot \gamma^2 \cdot \beta^2 \tag{1.29}$$

$$K = 2\pi \cdot N_A \cdot r_e^2 \cdot m_e \cdot c^2 \cdot z^2 \cdot (Z/A) \cdot (1/\beta^2). \tag{1.30}$$

Short Bethe–Bloch formula:

$$-\frac{dE}{dx} = 2K \cdot \left[\ln \frac{E_{\max}}{I} - \beta^2 - \frac{\delta}{2}\right]. \tag{1.31}$$

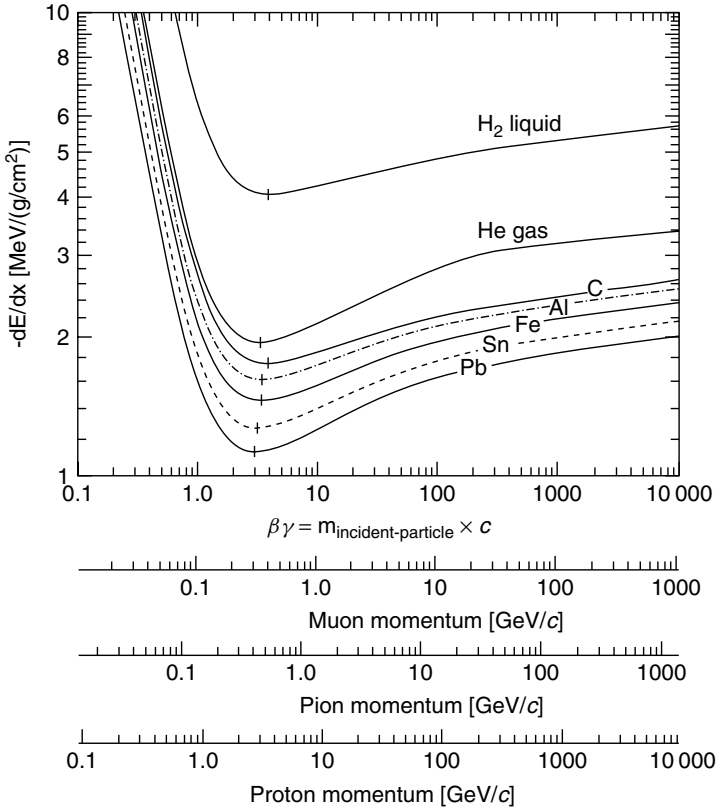

Fig. 1.19 The energy loss rate $-dE/dx$ in liquid hydrogen, helium gas, carbon, aluminum, tin, and lead (after Yao et al. [19] and Barnett et al. [97]).

The energy loss $-\frac{dE}{dx}$ is usually given by the dimension $\left(\frac{\text{MeV}}{\text{g/cm}^2}\right)$. However, usually the unit length dx is applied in (g/cm^2), because the energy loss per distance ds in cm, the so-called *mass thickness*, with $dx = \rho \cdot ds$ and density ρ in (g/cm^3), is weakly dependent of the material properties shown in the minimum of the stopping power functions of Figure 1.19. Equation (1.27) is only an approximation for the energy loss of charged particles in matter, but up to incident particle energies of several GeV predictions of the energy loss may have an accuracy of about several percent.

The differences in stopping power for some materials such as H, He, C, Al, Fe, Sn, and Pb are given in Figure 1.19. The stopping power functions show very broad minima at around $\beta\gamma = 3.0$ for a Z from 6 to 100. In most practical cases relativistic particles – energies of several GeV – have energy loss values close to the minimum of their stopping power functions. They define the so-called *minimum ionizing particles*, or *mips* .

The integration of Eq. (1.27) or (1.31) yields the total range R for a particle which loses energy through ionization. dE/dx depends only on β, whereas the range R

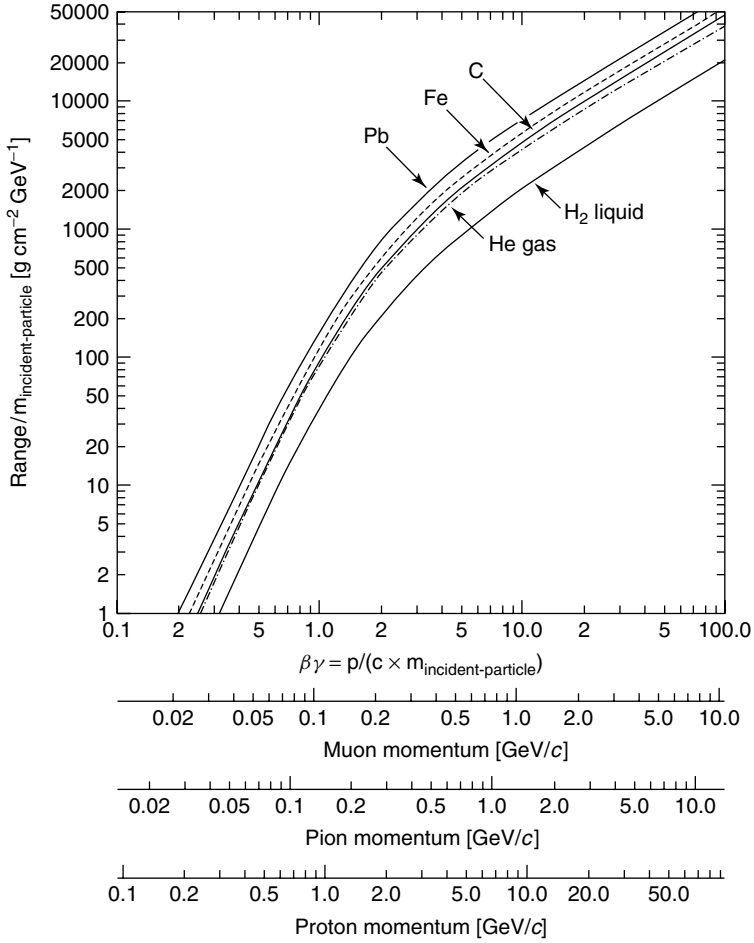

Fig. 1.20 Range of charged particles – protons, pions, and muons – in liquid hydrogen, helium gas, carbon, iron, and lead. As an example: a proton incident on lead with a momentum 1 GeV/c, a mass $m_{\text{incident-particle}} = 0.938$ (MeV/c^2), and $\beta\gamma = 1.066$. One may read $R/m_{\text{proton}} \approx 195\,\text{g cm}^{-2}\,\text{GeV}^{-1}$, and this is a range $R \approx 195\,\text{g cm}^{-2}$ or $R \approx 17.1$ cm (after Yao et al. [19] and Barnett et al. [97]).

divided by the incident particle mass m is a function of the energy E divided by the incident particle mass $m_{\text{incident-particle}}$ or of $p \cdot c/m_{\text{incident-particle}}$ with $p = \beta \cdot \gamma$ as the laboratory momentum of the incident particle in (GeV/c).

The range R per incident particle mass m is a function of $\beta\gamma = p \cdot c/m_{\text{incident-particle}}$ is given in Figure 1.20 for the materials liquid H, He gas, C, Fe, and Pb.

Carpenter [56] gives a reasonably accurate semiempirical formula (1.32) for the range R of protons in spallation source target materials, which is helpful to estimate

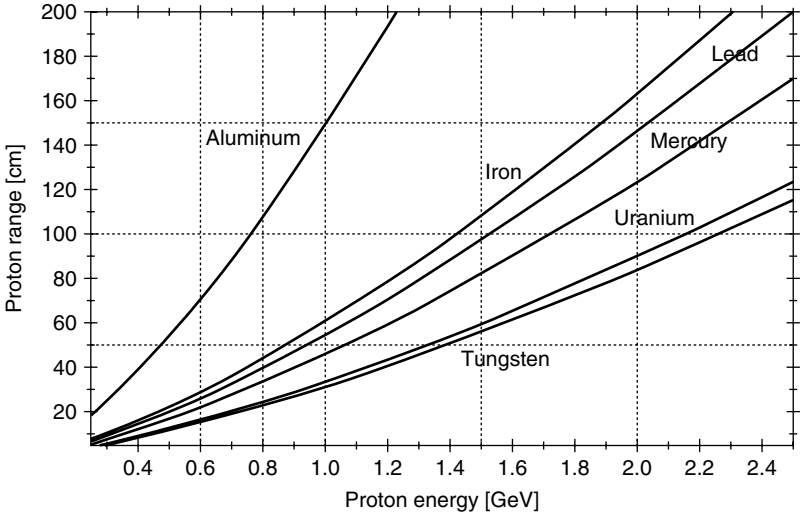

Fig. 1.21 Proton ranges in (cm) as a function of different incident proton energies on spallation target materials for Al, Fe, W, Hg, Pb, and U using Eq. (1.32).

the transversal dimensions of target systems. Neutrons are not uniformly produced in the target, and are spread out over a distance comparable with the range R of protons in the target material:

$$R(E_{\text{proton}}) = (1/\rho) \cdot 233 \cdot Z^{0.23}(E_{\text{proton}} - 0.032)^{1.4} \tag{1.32}$$

for $Z \geq 10$, $0.1 \leq E \leq 1$ GeV, $\rho =$ density in g/cm^3, and $E_p =$ incident proton energy in GeV. R has the dimension (cm) in Eq. (1.32) or if multiplied by ρ the dimension (g/cm^2).

Calculations using Eq. (1.32) are shown in Figure 1.21 and Table 1.13 for the ranges of protons for different incident energies in spallation target materials.

Other than for electrons, the range for charged hadrons is mainly dominated by energy loss due to ionization. Curves and tabulations of the range due to ionization exist for many different particles in different materials (see [97]). As mentioned earlier, Eq. (1.27) determines only the average energy loss of charged particles by ionization and excitation. Especially for thin targets – particularly for thin absorber layers – due to $dx = \rho \cdot ds$, fluctuations in the energy loss result in a distribution at the end of the range for the particles, which is called *range straggling* (cf. Section 4.4). This probability distribution is a Landau distribution [75], which describes the fluctuations around the mean energy loss. The Landau distribution about the mean value is asymmetric, with a tail extending to values much greater than the average.

1.3.6.2 **Coulomb Scattering**

A charged particle traversing a medium is deflected by many scatters, mostly at small angles. It will be scattered due to the interaction with the Coulomb potential

Tab. 1.13 Numerical values of ranges for protons incident on different spallation target materials calculated by using Eq. (1.32) (the properties of the materials are given in Table 1.12).

Incident proton energy E_p (GeV)	**0.4**	**0.6**	**0.8**	**1.0**	**1.5**	**2.0**
Carbon range (cm)	38.2	70.2	107.1	148.1	265.3	399.9
Aluminum range (cm)	38.4	70.5	107.6	148.7	266.5	401.6
Iron range (cm)	15.6	28.6	43.7	60.4	108.2	163.1
Copper range (cm)	13.9	25.6	38.9	53.9	96.6	145.6
Tungsten range (cm)	8.0	14.7	22.5	31.0	55.6	83.8
Mercury range (cm)	11.6	21.3	32.5	44.9	80.5	121.4
Lead range (cm)	13.0	25.6	39.1	54.0	96.8	145.9
Uranium range (cm)	8.6	15.8	24.0	33.2	59.5	89.8

of the nuclei, and to a lesser degree, to the fields of the electrons of the atoms. As Eq. (1.27) indicates, dE/dx is inversely proportional to the target mass, so that in comparison with electrons, the energy lost in Coulomb collisions with nuclei is negligible. However, for hadronic incident particles and for large target masses, a transverse *scattering* is appreciable in the Coulomb field of the nucleus. This is described by the Rutherford formula for the differential cross section at scattering angle Θ given by Eq. (1.33). This results in many small-angle scatters and is called multiple *Coulomb scattering*:

$$\frac{d\sigma(\Theta)}{d\Omega} = \frac{1}{4} \cdot \left(\frac{Z \cdot z \cdot e^2}{\beta \cdot c \cdot p} \right)^2 \cdot \frac{1}{\sin^4(\Theta/2)}, \tag{1.33}$$

where p is the momentum in (MeV/c^2), βc is the velocity, z is the charge of the incident particle, and Z is the charge of the nucleus, assumed to act as a point charge. The scattering distribution is described by Molière's theory [19, 98, 99] and approximates the projected scattering angle of multiple scattering by a Gaussian with a width of Θ^2_{rms}. The resultant distribution of the multiple scattering for small

deflections with a root-mean-square (rms) deflection in a layer x of a medium is given by

$$\Theta_{\mathrm{rms}} = \sqrt{\langle \Theta^2 \rangle} = \frac{13.6\ \mathrm{MeV}}{\beta \cdot c \cdot p} \cdot z \cdot \sqrt{\frac{x}{X_0}} \cdot \left[1 + 0.038 \cdot \ln(x/X_0)\right], \tag{1.34}$$

with the parameters defined above, x the depth of the traversed medium, and x/X_0 the thickness of the scattering medium in units of the radiation length. The value of Θ_{rms} may be determined by a fit to a Molière distribution [19, 99] for single charged particles with $\beta = 1$ for all Z, and is accurate to 11% or better for $10^{-3} < x/X_0 < 100$. The value of X_0 is determined by the formula (1.35) with Z and A the charge and the atomic mass of the absorber or target medium, respectively, and α the fine structure constant $\alpha = e^2/4 \cdot \pi \cdot \varepsilon_0 \cdot \hbar \cdot c = 1/137.566$ as given in Ref. [19]:

$$X_0 = \frac{A}{4 \cdot \alpha \cdot N_A \cdot Z^2 \cdot r_e^2 \cdot \ln(183 \cdot Z^{-1/3})} \left(\mathrm{g/cm^2}\right). \tag{1.35}$$

Equation (1.34) is an approximation and is written for practical purposes using particles with $z = 1$ in the following form:

$$\Theta_{\mathrm{rms}} = \sqrt{\langle \Theta^2 \rangle} = \frac{13.6\ \mathrm{MeV}}{\beta \cdot c \cdot p} \cdot \sqrt{\frac{x}{X_0}}. \tag{1.36}$$

Coulomb scattering is important in practice because it limits the precision with which the direction of charged particles in particle beam interactions with thick targets in spallation applications can be determined.

1.3.6.3 **Bremsstrahlung**

In addition to the ionization loss high-energy charged particles lose energy in interactions with the Coulomb field of the nuclei of the medium. If charged particles are de-accelerated in the Coulomb field, one part of the particle's kinetic energy will be emitted as photons called *bremsstrahlung*. The energy loss due to bremsstrahlung is determined (see [96]):

$$-\frac{dE}{dx} = 4 \cdot \alpha \cdot N_A \cdot \frac{Z^2}{A} \cdot z^2 \cdot \left(\frac{1}{4\pi\varepsilon_0}\frac{e^2}{mc^2}\right)^2 \cdot E \cdot \ln\left(\frac{183}{Z^{1/3}}\right), \tag{1.37}$$

where Z and A are atomic number and atomic mass of the medium, and z, m, and E are the atomic number, mass, and energy of the incident particle, respectively.

The energy loss due to bremsstrahlung for electrons is determined as

$$-\frac{dE}{dx} = 4 \cdot \alpha \cdot N_A \cdot \frac{Z^2}{A} \cdot r_e^2 \cdot E \cdot \ln\left(\frac{183}{Z^{1/3}}\right) \quad \left(\frac{\mathrm{MeV}}{\mathrm{g/cm^2}}\right) \tag{1.38}$$

if $E \gg m_e \cdot c^2/\alpha \cdot Z^{1/3}$.

Remarkable is the difference compared to the ionization loss of Eq. (1.27). The bremsstrahlung loss is proportional to the energy and inversely proportional to the squared mass of the incident particle, whereas the ionization loss beyond the minimum ionization is proportional to the logarithm of the energy. At the so-called critical energy E_c the average energy loss by bremsstrahlung and by ionization is the same:

$$-\frac{dE}{dx}(E_c)|_{\text{ionization}} = -\frac{dE}{dx}(E_c)|_{\text{bremsstrahlung}}. \tag{1.39}$$

The critical energy E_c could be evaluated using Eqs. (1.27) and (1.37). The critical energy E_c is approximately given for media with $Z \geq 13$ [19, 85] as

$$E_c = \frac{(500)\ \text{MeV}}{Z} \tag{1.40}$$

with Z the atomic number of the target material. The accuracy of approximate forms for E_c of Eq. (1.40) is limited by different media – gases, liquids, and solids –, which have substantial differences in ionization at the relevant energy because of density fluctuation effects [19].

1.3.6.4 Energy Loss by Direct Pair Production and by Photonuclear Interaction

There exist two additional energy loss mechanisms if high-energy charged particles interact with matter. By traversing the Coulomb field of the target nucleus high-energy particles may produce electron–positron pairs by virtual photons or the charged particles lose energy by virtual photon exchange undergoing nonelastic collisions. These energy losses are proportional to the incident particle energy. An instructive example is given for muons at 100 GeV incident on iron where the following approximation is valid:

$$-\frac{dE}{dx}|_{\text{pair production}} = 0.3\left(\frac{\text{MeV}}{\text{g/cm}^2}\right) \tag{1.41}$$

$$-\frac{dE}{dx}|_{\text{photonuclear}} = 0.04\left(\frac{\text{MeV}}{\text{g/cm}^2}\right) \tag{1.42}$$

Details are given in [89] and references therein.

1.3.6.5 Total Energy Loss

The total energy loss of charged particles can be determined as the sum of the individual losses as ionization, bremsstrahlung, pair production, and photonuclear interactions:

$$\begin{aligned} -\frac{dE}{dx}|_{\text{total}} = &-\frac{dE}{dx}|_{\text{ionization}} - \frac{dE}{dx}|_{\text{bremsstrahlung}} \\ &-\frac{dE}{dx}|_{\text{pair production}} - \frac{dE}{dx}|_{\text{photonuclear}}. \end{aligned} \tag{1.43}$$

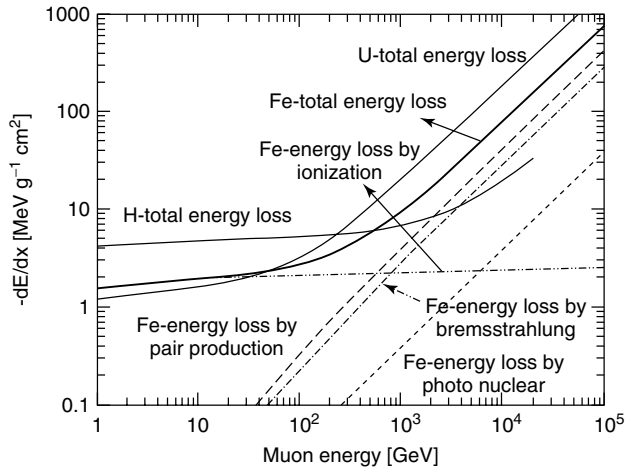

Fig. 1.22 Average energy loss of a muon in hydrogen, iron, and uranium as a function of energy. For iron the different contributions to dE/dx as ionization, bremsstrahlung, pair, and photonuclear production are also shown [19].

At sufficiently high energies radiative processes become more important for all charged particles. In Figure 1.22, this is shown for muons of energies from 1 GeV to about 10^5 GeV incident on hydrogen, iron, and uranium [19, 99]. Note that the energy scale in this figure is beyond the energy generally discussed in the framework of neutron spallation sources or currently discussed in accelerator-driven applications.

1.3.7
High-Energy Hadronic Cascades and Nuclear Interactions

Nonelastic collisions are important in predicting high-energy hadronic cascades, and it is the interaction mechanism, that is least understood and has the largest physics uncertainties. Some qualitative features of nonelastic hadron–nucleus collisions will be discussed. Elastic hadron–nucleus interactions are characterized by very small energy losses and small angular deflections. They can often be neglected in calculating the effects of hadronic cascades in thick targets. But there are several situations in narrow beam sources, accelerator shielding, high-energy physics calorimeters, heat deposition, etc., where elastic scattering effects may be important. The total cross sections, some useful semiempirical expressions, and double differential cross sections will be discussed in Sections 1.3.7.4 and 1.3.7.6.

1.3.7.1 Qualitative Features of Hadron–Nucleus Collisions

Some qualitative features of hadron nucleus collisions which often allow significant simplifications in predicting thick target cascades are as follows:

- Above about a few 100 MeV, the total elastic and nonelastic cross sections are approximately constant; for an example see Figure 1.23.

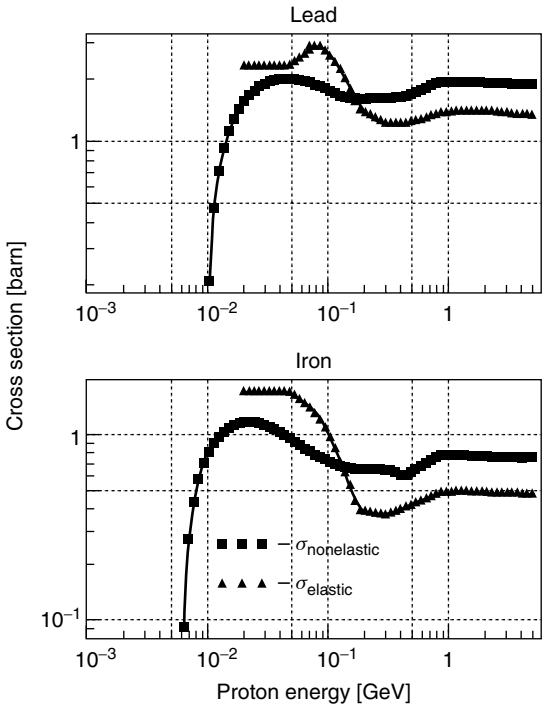

Fig. 1.23 Example of elastic and nonelastic proton nucleus cross sections for Fe and Pb as a function of the incident proton energy of about $E > 10^{-2}$ GeV calculated by GEANT4 [100].

- For high-energy particles produced in hadron–nucleus collisions, the perpendicular momentum is much smaller than the parallel momentum (i.e., the secondary particle direction is approximately "straight ahead" relative to the incident particle direction), and the perpendicular momentum component increases slowly with increasing incident particle momentum.
- The multiplicity of high-energy particles created increases slowly with increasing kinetic energy E of the incident particle, roughly as $\ln(E)$.
- The residual excitation energy, and hence, low-energy particle multiplicities, left after the high-energy particle production increases linearly with the energy of the incident particle.

Examples of these general characteristics can be found in the literature [101–104] and will be shown and discussed in Part 2 on page 277.

1.3.7.2 **Characteristics of Hadron Cascades in Thick Targets**

The main features of high-energy hadronic cascades generated in matter are demonstrated in Figure 1.24. The generation of a hadronic cascade in a thick target is characterized by an initial increase in particle flux intensity with depth due to

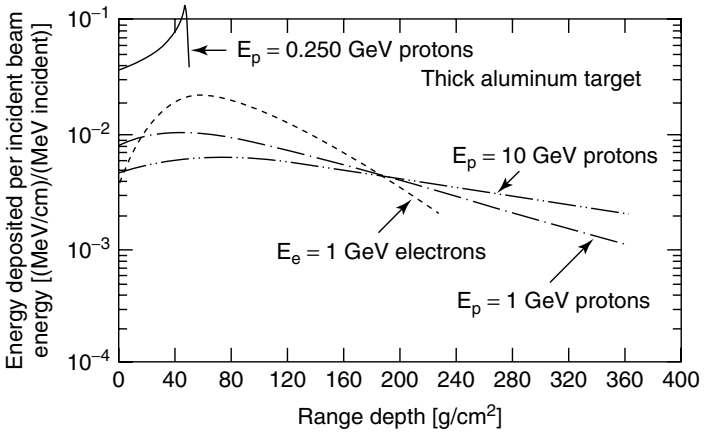

Fig. 1.24 Energy deposition per unit incident beam energy produced in a semiinfinite aluminum target by proton and electron beams (after Armstrong [105]).

secondary particle production, followed by a gradual decline as the average energy of the cascade particles decreases, multiplicities decrease, and a greater fraction of individual particle energies is dissipated by ionization losses. Figure 1.24 shows the depth dependence of the energy deposition produced in a semiinfinite aluminum target by 0.250, 1, and 10 GeV proton beams, respectively, and for comparison, a 1 GeV electron beam.

At 0.250 GeV the proton range of about 50 g/cm^2 is less than the mean free path for nuclear collisions, so most of the protons stop without undergoing collisions, and the energy deposition curve exhibits a so-called Bragg peak. For the 1 and 10 GeV example, nuclear collisions occur before the stopping range is reached, and the deposition curves show the characteristics of well-developed hadronic cascades.

1.3.7.3 Spatial Propagation of Hadron Cascades and Particle Production

For incident particle beam energies of about $E_{\text{nucleon}} \leq 10$ GeV, the most penetrating component in the cascade is usually nucleons-proton and neutron-above a few hundred MeV. High-energy neutrons are particularly important since the protons will be degraded by ionization losses and lower energy neutrons have smaller mean free paths. For depths greater than a few mean free paths, the effective cascade attenuation length approaches a relatively constant value, and e.g., the shape of the neutron spectrum varies weakly with depth. These phenomena are briefly described in the following.

- *Pion production*: For incident particle energies of about $E_{\text{nucleon}} \geq 10$ GeV, pion production becomes important. The charged pions do not have a major effect on the spatial propagation of the cascade because of their soft production spectrum. However, they may be an important contributor to energy deposition and an important muon source. Neutral pions are usually not a major component for

the spatial propagation of the cascade because the radiation length in matter for the electromagnetic cascade initiated by the high-energy photons from π^0-decay is typically much less than the hadronic cascade attenuation length. However, neutral pions will become important contributors to energy deposition for pion energies $E_{\text{pion}} \geq 10$ GeV, and will provide the dominant deposition mechanism above 100 GeV in hadron cascades.

- *Muon production*: For incident particle energies of about $E_{\text{nucleon}} \geq 10$ GeV, muon production becomes important, and, since muons are degraded only by ionization losses at about $E_{\text{muon}} \leq 100$ GeV, they become the dominant cascade component at very large depths for energies of about $E_{\text{muon}} \geq 100$ GeV. For energies above 10 GeV, muons may be abundant, particularly for cases where (a) the target material is of low density (e.g., air or other gaseous products) where pions predominately decay rather than interact, or (b) in dense materials (e.g., Fe, Pb, etc.) at large depths after the hadronic cascade has diminished.
- *Kaon production*: The kaon production in nuclear collisions is typically about 1/10 of the pion production. Where muons are of interest in applications, the kaons may provide an important background source because they decay faster than pions.

1.3.7.4 Total Cross Sections in Nucleon–Nucleus Collisions

As mentioned earlier, the interaction of high- and intermediate-energy protons in matter is of much interest. The fundamental observable is the *total reaction cross section*, which is defined as the difference between the total cross section and the total elastic cross section:

$$\sigma_{\text{reaction}} = \sigma_{\text{total}} - \sigma_{\text{elastic}} \sim \sigma_{\text{total-nonelastic}}. \tag{1.44}$$

Various semiempirical expressions and formulas have been derived for the total elastic and total-nonelastic cross sections, and for the mean free path for nonelastic collisions of protons incident on different target nuclei [90, 91, 106, 107]. The semiempirical expressions are usually derived by fitting existing experimental data [87, 108, 109]:

$$\begin{aligned} \sigma_{\text{total-elastic}} &\approx 6 \cdot A \quad \text{(mb)} \\ \sigma_{\text{total-nonelastic}} &\approx a \cdot A^{2/3} \quad \text{(mb)} \\ \lambda_{\text{meanfp}} &\propto A^{1/3}, \end{aligned} \tag{1.45}$$

where $a \approx 30$ (mb) for $A = 1$, and $a \approx 50$ (mb) for $A > 1$. For neutrons and pions, the nonelastic cross sections are smaller by about 10% and 20%, respectively. The mean free path λ_{meanfp} for nonelastic interactions is not very dependent upon material it is varying only from ~100 to ~200 (g/cm^2) from aluminum to lead or uranium. This is also shown in Table 1.12. The very simple semiempirical formulas for the total-nonelastic cross section of Eq. (1.45) were further refined and tuned by fitting experimental data (see Refs. [91, 107]).

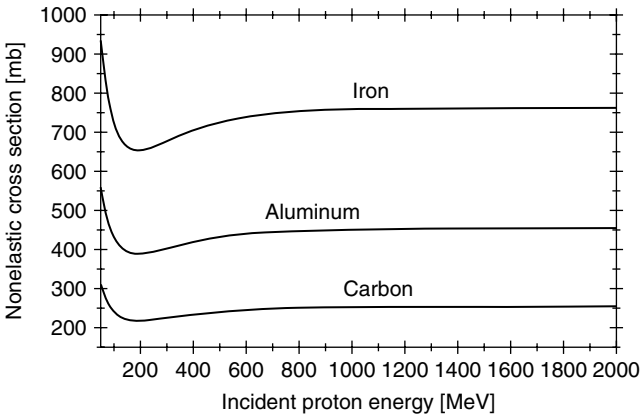

Fig. 1.25 Calculated semiempirical total-nonelastic cross sections for C, Al, and Fe using formula (1.46).

The Letaw formula Letaw et al. [107] have published a formula for proton–nucleus nonelastic cross sections for incident proton energies $E > 10$ MeV as follows:

$$\sigma(E)_{\text{nonelastic}} = \sigma_{\text{high-energy}} \cdot \left[1 - 0.62 \cdot \exp(-E/200) \cdot \sin(10.9 \cdot E^{-0.28)}\right] \text{(mb)},$$
$$\text{with} \quad \sigma_{\text{high-energy}} = 45 \cdot A^{0.7} \cdot \left[1 + 0.016 \cdot \sin(5.3 - 2.63 \cdot \ln A)\right] \text{(mb)}, \tag{1.46}$$

where E is the energy of the incident proton in (MeV) and A is the atomic mass of the target nucleus. Two examples of calculations using the formula (1.46) are shown in Figures (1.25) and (1.26), respectively, for C, Al, Fe, W, Hg, Pb, and U.

At energies below 2 GeV the total-nonelastic cross section is not independent of energy. In general, the cross section sharply increases to a maximum at about 20 MeV and then decreases to a minimum at 200 MeV. Letaw et al. [107] have evaluated the uncertainties in the energy-dependent formula (1.46) comparing the results with experimental data and discussed the reasons of further refinements of the formula (1.46). The estimated maximum uncertainty for different energy ranges is listed in Table 1.14.

The Wellish formula Wellisch and Axen [91] have also specified a general formula for the total-nonelastic cross section named here as total reaction cross section for the energy range of protons from 6.8 MeV to 10 GeV for all target materials with $Z > 5$. This evaluation is based mainly on Ref. [90]. This formula as given by Eq. (1.47) is used as a basis for the hadronic package GEANT4 [100]. For the most important isotopes in accelerator-driven technologies (ADT) such as iron, tungsten, and lead, Prael and Chadwick evaluated the total-nonelastic cross section for neutrons and protons up to incident energies of 2 GeV [110–112]. These cross-section evaluations are applied in the LAHET code [113] and validate also the

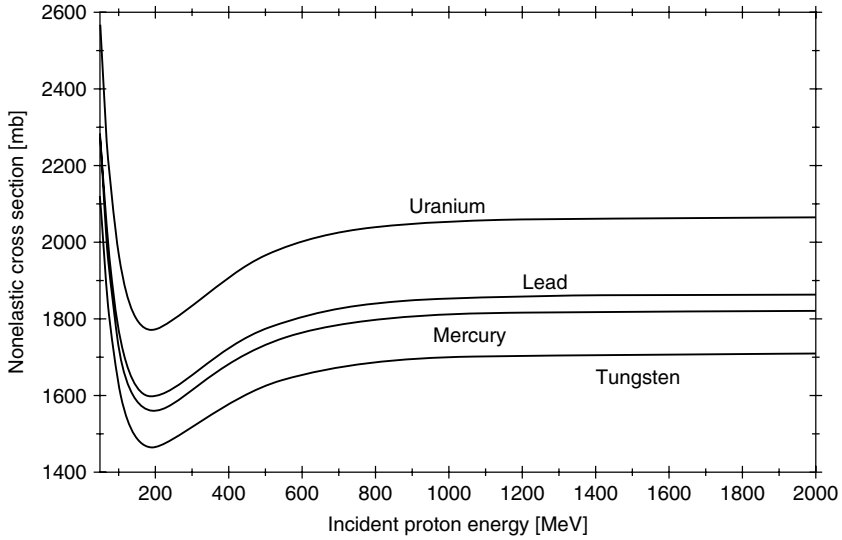

Fig. 1.26 Calculated semiempirical total-nonelastic cross sections for W, Hg, Pb, and U using formula (1.46).

Tab. 1.14 Errors in the energy-dependent formula (1.46).[a]

Energy range	Estimated maximum error (%)
$E > 1$ GeV	2
300 MeV $< E \leq 1$ GeV	5
100 MeV $< E \leq 300$ MeV	10
40 MeV $< E \leq 100$ MeV	20
10 MeV $< E \leq 40$ MeV	$\sim$ a factor of 2

[a] Mean errors are about 0.5 times the maximum errors

semiempirical formula of [91].

$$\sigma_{\text{total-nonelastic}} \sim \sigma_{\text{reaction}} = f_{\text{corr}} \cdot \pi \cdot r_0^2 \cdot \ln N \cdot [1 + A^{1/3} - b_0(1 - A^{-1/3}), \tag{1.47}$$

with N the number of neutrons in the target, A the atomic mass, and b_0 and r_0 defined as published in [90]:

$$\begin{aligned} b_0 &= 2.247 - 0.915 \cdot (1 + A^{1/3}), \\ r_0 &= 1.36 \text{ fm} = 1.36 \times 10^{-13} \text{ cm}, \\ f_{\text{corr}} &= \frac{1+0.15\cdot\exp(-E_{\text{kin}})}{1+0.0007\cdot A}. \end{aligned} \tag{1.48}$$

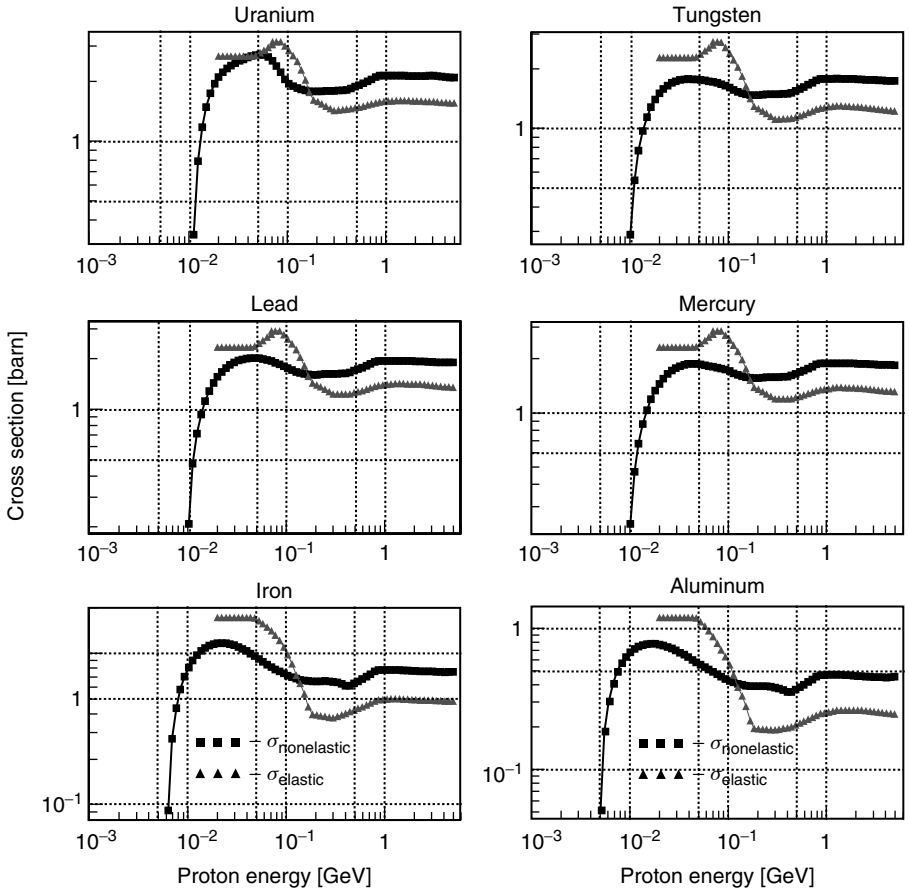

Fig. 1.27 Representative examples of total-elastic and total-nonelastic proton nucleus cross sections for Al, Fe, W, Hg, Pb, and U as a function of the incident proton energy in the MeV–GeV range calculated by GEANT4 [100].

In Figure 1.27 examples of total-elastic and total-nonelastic cross sections as determined by GEANT4 for Al, Fe, W, Hg, Pb, and U target materials of relevance for spallation reaction applications are depicted.

A very useful source of evaluated experimental values as total cross sections, elastic cross sections, and nonelastic cross sections of interaction of neutrons and protons for many different target materials from deuterium to uranium nuclei is given in Refs. [87, 108, 109]. Only published data have been included. There are clearly gaps in energy and in target material in the data. Representative examples of the data are shown in Figures 1.28, 1.29, 1.30. The uncertainty of the measured data is mostly about $1\sigma = \pm 10\%$ at incident proton energies $E \geq 200$ MeV and is within the size of the plotted symbols. Measurements of the total reaction cross section in connection with the development of high power spallation sources were recently

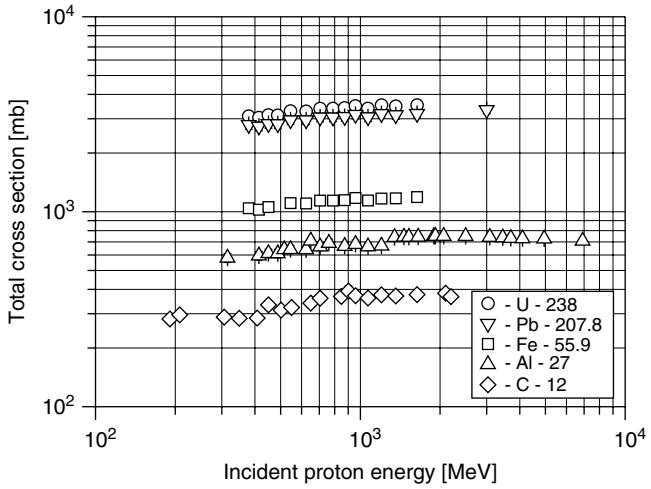

Fig. 1.28 Examples of experimental values – uncertainty about $1\sigma = \pm 10\%$ – of proton-induced total cross sections from [108, 109].

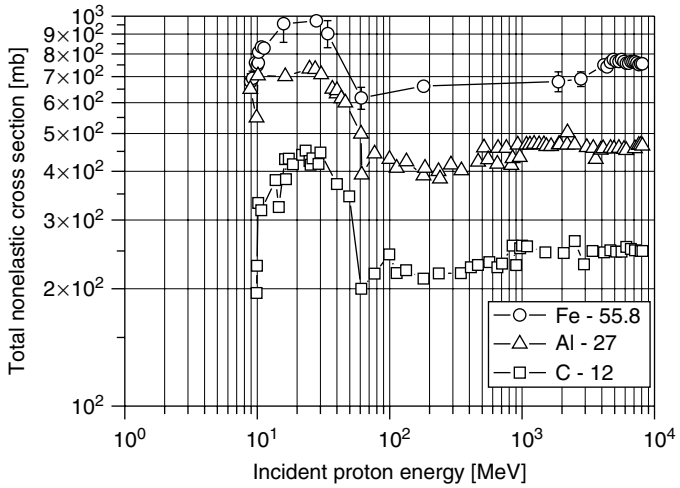

Fig. 1.29 Examples of experimental values – uncertainty about $1\sigma = \pm 10\%$ – of proton-induced total-nonelastic cross sections of C, Al, and Fe from [108, 109].

reported in [114, 115]. These measurements give similar results as summarized in [87, 108, 109] (Table 1.15).

As an example, the elastic scattering cross sections for protons are shown for the materials C, Al, Fe, and Pb in Figure 1.31 evaluated from Cloth et al. [88] (cf. elastic scattering of neutrons and protons in Chapter 4, Section 4.5).

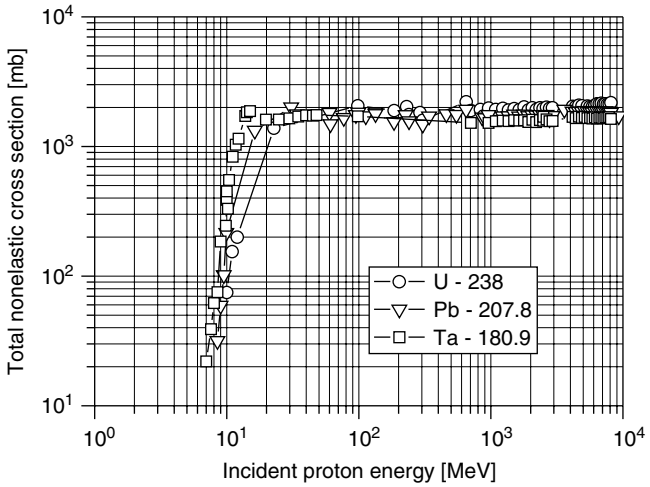

Fig. 1.30 Examples of experimental values – uncertainty about $1\sigma = \pm 10\%$ – of proton-induced total-nonelastic cross sections of Ta, Pb, and U from [108, 109].

Tab. 1.15 Comparison of measured and theoretical evaluated nonelastic cross sections at an incident proton energy of $E = 1.2$ GeV.

References	Target element	Total reaction cross section/ Total nonelastic cross section (mb) $\pm 1\sigma$ (mb)
Barashenkov [108]	Pb	1713 ± 103
	U	1975 ± 119
Enke et al. [114]	Pb	1780 ± 125
	U	1730 ± 121
Letourneau et al. [115]	Pb	1650 ± 30
	U	–
Letaw[a] et al. [107]	Pb	1850 ± 16
	U	2090 ± 45
Wilson[b] et al. [116]	Pb	1693 ± 150
Cugnon model INCL 4.3 [117]	Pb	1801 ± 16
	U	2013 ± 45

[a] Semiempirical formula.
[b] Calculations by means of a high-energy heavy-ion model.

1.3.7.5 Total Reaction Cross Sections in Nucleus–Nucleus Reactions

The transportation of light and heavy ions in matter is of much interest in science. The total reaction cross sections have been studied both experimentally and theoretically. Several empirical parameterizations as derived for nucleus–nucleus

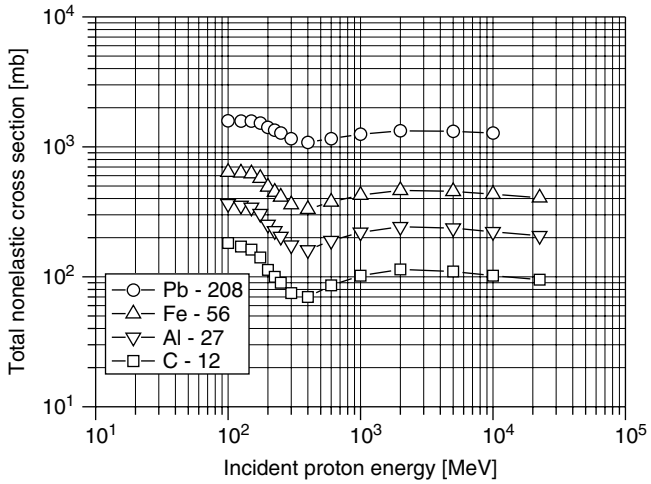

Fig. 1.31 Examples of proton-induced total elastic cross sections – uncertainty about $1\sigma = \pm 10\%$ – for C, Al, Fe, and Pb evaluated in [88, 116] in the energy range from 0.1 to 22.5 GeV.

collisions (cf. Section 1.3.7.4) are given in the references by Sihver et al. [90], Kox et al. [118], and Tripathi et al. [119–121] and the citations therein.

As given in Section 1.3.7.4, the total reaction cross section $\sigma(N, N)_R$ is defined as

$$\sigma(N, N)_R = \sigma_{\text{total}} - \sigma_{\text{elastic}} \tag{1.49}$$

with σ_{total} the total cross section and σ_{elastic} the elastic cross section.

The Sihver formula The formula of Sihver et al. [90] is in its simplest form similar to Eq. (1.46), the formula of Letaw et al. [107]:

$$\sigma(N, N)_R = \pi \cdot r_0^2 \left[A_{\text{projectile}}^{1/3} + A_{\text{target}}^{1/3} - b_0 \left[A_{\text{projectile}}^{-1/3} + A_{\text{target}}^{-1/3} \right] \right]^2, \tag{1.50}$$

where $A_{\text{projectile}}$ and A_{target} are the atomic mass numbers of the projectile and the target nuclei, respectively, $r_0 = 1.36$ fm and b_0 is given by

$$b_0 = 1.581 - 0.876 \left(A_{\text{projectile}}^{-1/3} + A_{\text{target}}^{-1/3} \right). \tag{1.51}$$

The formula consists of a geometrical term $(A_{\text{projectile}}^{1/3} + A_{\text{target}}^{1/3})$ and a transparency parameter b_0 for the nucleons in the nucleus. It is assumed that the cross section is independent of incident energies ≥ 100 MeV/nucleon. The formula gives a good agreement with experimental data for most of the collision systems, which have been studied (see Ref. [90]).

In the case of nucleon–nucleus interactions, formula (1.50) is almost identical for proton–nucleus (with $Z_{\text{target}} \leq 26$) if $A_{\text{projectile}} = 1$ is a proton and the parameter b_0

is expressed as a polynomial function of the first order in $(1 + A_{\text{target}}^{-1/3})$. The formula then becomes

$$\sigma(p, N)_R = \pi \cdot r_0^2 \left[1 + A_{\text{target}}^{1/3} - b_0[1 + A_{\text{target}}^{-1/3}]\right]^2$$
$$b_0 = 2.247 - 0.915\left(1 + A_{\text{target}}^{-1/3}\right) \tag{1.52}$$

for incident proton energies $E_{\text{proton}} \geq 200$ MeV and $r_0 = 1.36$ fm.

The Kox formula The Kox formula in Ref. [118] is based on the strong absorption model to describe low-energy nuclear reactions. The formula is based on the analysis of total reaction cross sections for heavy ion collisions in the intermediate-energy range of about 10–300 MeV/nucleon. The formula determines the total reaction cross section $\sigma(N, N)_R$ in terms of the interaction radius IR, the nucleus–nucleus interaction barrier B_C, and the center-of-mass energy $E_{\text{c.m.}}$ of the colliding system. In this framework it is considered that a reaction occurs whenever a substantial contact occurs between nuclear matter. The formula is given in its general form as

$$\sigma(N, N)_R = \pi(IR)^2[1 - B_C/E_{\text{c.m.}}]. \tag{1.53}$$

The parameter B_C is the Coulomb barrier of the projectile–target system. It is given by

$$B_C = \left(Z_{\text{projectile}} \cdot Z_{\text{target}} \cdot e^2\right) / \left(r_C(A_{\text{projectile}}^{1/3} + A_{\text{target}}^{1/3})\right), \tag{1.54}$$

where $r_C = 1.3$ fm, e is the electron charge, $Z_{\text{projectile}}$ and Z_{target} are the atomic numbers of the projectile and the target nuclei, and $A_{\text{projectile}}$ and A_{target} are the atomic masses of the projectile and the target nuclei, respectively. The interaction radius IR is divided in the Kox formula into volume and surface terms, R_{vol} and R_{surf}:

$$IR = R_{\text{vol}} + R_{\text{surf}}. \tag{1.55}$$

The terms R_{vol} and R_{surf} correspond to energy-independent and energy-dependent components of the reactions, respectively. Collisions with smaller impact parameters are independent of energy and mass number and are characterized as a volume component of the interaction radius and therefore depends only on the volume of the projectile and the target nuclei. It is given by

$$R_{\text{vol}} = r_0(A_{\text{projectile}}^{1/3} + A_{\text{target}}^{1/3}). \tag{1.56}$$

The second term of the interaction radius IR in Eq. (1.55) is a nuclear surface contribution and is parameterized by

$$R_{\text{surf}} = r_0\left[a \cdot \frac{A_{\text{projectile}}^{1/3} \cdot A_{\text{target}}^{1/3}}{A_{\text{projectile}}^{1/3} + A_{\text{target}}^{1/3}} - c\right] + D. \tag{1.57}$$

The first term in the brackets is the mass asymmetry term, which is related to the volume overlap of the projectile and the target. The second term c is an energy-dependent parameter, which takes into account the increasing surface transparency as the projectile energy increases. The parameter D is the neutron excess which is important in collisions with heavy or neutron-rich targets. It is given by

$$D = \frac{5(A_{\text{target}} \cdot Z_{\text{target}})Z_{\text{projectile}}}{A_{\text{projectile}} \cdot A_{\text{target}}}. \tag{1.58}$$

The parameters $r_0 = 1.1$ fm and $a = 1.85$ are fixed values where the parameter c is a function of the beam energy per nucleon which is a simple analytical function derived from Ref. [118] and used in *GEANT4* [100] to

$$\begin{aligned} c &= -\frac{10}{x^5} + 2.0 && \text{for } x \geq 1.5, \\ c &= \left(-\frac{10}{1.5^5} + 2.0\right) \cdot \left(\frac{x}{1.5}\right)^3 && \text{for } x < 1.5, \\ x &= \log(E_{\text{kin}}), \end{aligned} \tag{1.59}$$

where E_{kin} is the kinetic projectile energy in units MeV/nucleon in the laboratory system.

The Tripathi formula For nucleon–nucleon and nucleus–nucleus interactions Triphati et al. [119–121] have proposed alternative algorithms for calculating the interaction cross sections. The formula is a simple universal parameterization of the total reaction cross section for any system of colliding nuclei valid for the entire energy range from a few A MeV to a few A GeV. This approach treats the proton–nucleus collision as a special case of the nucleus–nucleus collision, where the projectile has charge and mass number 1. Parameters to treat the Coulomb interaction at lower energies and modifications of the reaction cross section at higher energies due to the Pauli blocking are also taken into account:

$$\sigma(N,N)_R = \pi r_0^2 \cdot \left[A_{\text{projectile}}^{1/3} + A_{\text{target}}^{1/3} + \delta_E\right]^2 \cdot \left[1 - \frac{B}{E_{\text{c.m.}}}\right], \tag{1.60}$$

where $r_0 = 1.1$ fm. In formula (1.60) the parameter B, the energy-dependent Coulomb barrier, and R are given by

$$B = 1.44 \cdot \frac{Z_{\text{projectile}} \cdot Z_{\text{target}}}{R}, \tag{1.61}$$

$$R = r_{\text{projectile}} + r_{\text{target}} + \frac{1.2 \cdot \left[A_{\text{projectile}}^{1/3} + A_{\text{target}}^{1/3}\right]}{E_{\text{c.m.}}^{1/3}}, \tag{1.62}$$

where r_i is the equivalent sphere radius and is related to the $r_{\text{rms},i}$ radius by $r_i = 1.29 \cdot r_{\text{rms},i}$ with $i =$ projectile, target), and $E_{\text{c.m.}}$, the center of mass energy, is given in MeV.

There is an energy dependence of the reaction cross section at intermediate and higher energies mainly due to two effects, the transparency and the Pauli blocking [119]. This is represented by the energy-dependent term δ_E in formula (1.60) given as

$$\begin{aligned}
\delta_E &= 1.85 \cdot S_1 + 0.16\frac{S_1}{E_{\text{c.m.}}^{1/3}} - C_E + 0.91 \cdot S_2 \\
S_1 &= \frac{A_{\text{projectile}}^{1/3} \cdot A_{\text{target}}^{1/3}}{A_{\text{projectile}}^{1/3} + A_{\text{target}}^{1/3}} \\
S_2 &= \frac{(A_{\text{target}} - 2Z_{\text{target}})Z_{\text{projectile}}}{A_{\text{projectile}} \cdot A_{\text{target}}},
\end{aligned} \tag{1.63}$$

where S_1 is the mass asymmetry term and is related to the volume overlap of the collision system and the term S_2 in the formula is related to the isotope dependence of the reaction cross section.

The term C_E in formula (1.63) is related to the transparency and the Pauli blocking and is given by

$$C_E = D_{\text{Pauli}} \cdot \left(1 - \exp\left(-\frac{E}{40}\right)\right) - 0,292 \cdot \exp\left(-\frac{E}{792}\right) \cdot \cos\left(0.229 \cdot E^{0.453}\right). \tag{1.64}$$

The parameter D_{Pauli} in formula (1.64) takes into account the density dependence of the colliding system, scaled with respect to the density of the (^{12}C +^{12} C) colliding system.

$$D_{\text{Pauli}} = 1.75 \cdot (\rho_{A_{\text{projectile}}} + \rho_{A_{\text{target}}})/(\rho_{A_C} + \rho_{A_C}), \tag{1.65}$$

where the density of a nucleus using the hard sphere model [122] with a given nucleus of mass number A_i is given by

$$\rho_{A_i} = A_i/\left(\frac{3}{4}\pi \cdot r_i^3\right), \tag{1.66}$$

where the radius of the nucleus r_i is defined above with the root-mean-square radius, $(r_i)_{\text{rms}}$, obtained directly from experimental data [123]. With the parameter D_{Pauli} simulates the modifications of the reaction cross section caused by the Pauli blocking which was introduced by Tripathi et al. [119] in the parameterization formula for the first time. At lower energies where the overlap of interacting nuclei is small and Coulomb interaction modifies the cross sections significantly, the influence of the Pauli blocking is small. The modification of the reaction cross section due to Pauli blocking plays an important role at energies above 100 Mev/nucleon in nucleus–nucleus collisions which lead to higher densities. For proton–nucleus collisions where the compression effect is low, a single constant value $D_{\text{Pauli}} = 2.05$ gives good results for all proton–nucleus collisions [119].

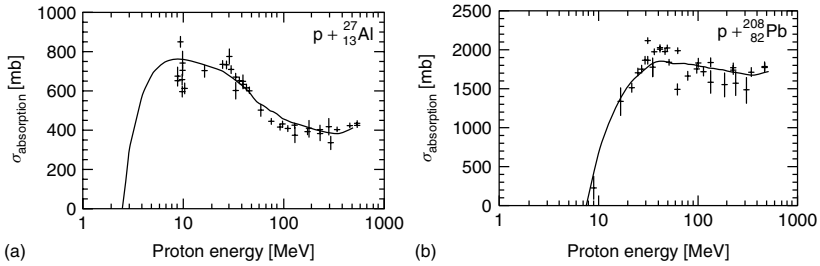

Fig. 1.32 Absorption cross section for proton–aluminum collisions (a) and proton–lead collisions (b) as a function of the incident proton energy. The experimental data points are from de Vries et al. [123]. The solid lines are the results of calculations given in Ref. [120] (after Tripathi et al. [120]).

For alpha–nucleus and lithium–nucleus collisions, where there is also little compression, the following terms for the D_{Pauli} parameter are useful:

$$\begin{aligned} D_{\text{Pauli}}(\alpha) &= 2.77 - (8.0 \times 10^{-3} \cdot A_{\text{target}}) + (1.8 \times 10^{-5} \cdot A_{\text{target}}^2) \\ &\quad - 0.8/[1 + \exp[(250 - E)/75]] \\ D_{\text{Pauli}}(\text{lithium}) &= D_{\text{Pauli}}/3 \quad (\text{see Eq. (1.65)}). \end{aligned} \tag{1.67}$$

Figure 1.32 shows as an example the results of calculations for the reaction cross sections for protons on Al and Pb targets of Ref. [120]. The experimental data have been taken from the compilation of Ref. [123]. The Tripathi formalism gives a very good agreement with the experimental data also for other collision systems for the entire energy range[1)].

1.3.7.6 **Differential Cross Sections**

As mentioned earlier, the cross section is an extremely important concept in describing the interaction of particles with matter. By definition the *angular differential cross section* $d\sigma/d\Omega$ is the derivative of σ to the solid angle Ω and is proportional to the probability of a reaction of an incident particle with a nucleus by emitting a secondary particle into a cone $d\Omega$. The differential cross section has the dimension barns/steradian (b/sr). Note the condition $\int (d\sigma/d\Omega) d\Omega = \sigma$, which makes it clear why $d\sigma/d\Omega$ is called the *angular differential cross section*. Another condition is to consider the incident particle to have a certain energy E and particles after interaction to have energy in an interval dE' about E'. This defines in a similar way as above an energy dependent differential cross section, $d\sigma/dE'$, which is a measure of the probability that an incident particle with incident energy E will have as a result of the interaction an outgoing energy E'. Both $d\sigma/d\Omega$ and $d\sigma/dE'$ are distribution functions; the former is a distribution in the variable Ω, the solid angle, whereas the latter is a distribution in E', the energy after scattering. Their dimensions are barns per steradian and barns per unit energy, respectively.

1) See comment in Section 2.5.1 on page 115.

Combining the two extensions above from the cross sections to differential cross sections, it follows a further extension to the so-called *double differential cross section*:

$$d^2\sigma/d\Omega\ dE(\mathrm{b\,sr^{-1}\,MeV^{-1}}), \tag{1.68}$$

which is a quantity that has been extensively studied in particle scattering. This cross section contains the most fundamental information about the structure and dynamics of particle–nucleus or particle–matter interactions and collisions. Measurements of double differential production cross sections provide a very sensitive observable for the validity of the spallation physics models. In the past systematic studies and measurements were investigated as part of the development of intense spallation neutron sources, for a new generation of meson factories, and for the theoretical understanding of medium energy physics in the energy range up to several GeV [124–132]. For *ADS* (accelerator-driven systems) projects [133] in references on the interaction of protons and neutrons mainly for lead targets are summarized. The experiments are discussed in Part 2 on page 277. There is still interest in medium-energy particle reaction data as double differential secondary production cross sections of charged particles, neutrons, pions, radioactive isotopes, etc., mainly for incident particles above 100 MeV. Some examples of semiempirical systematics on neutron spectra measurements [129, 130] from high-energy proton bombardment by 318, 590, and 800 MeV protons on eight targets in the mass range $A = 12$ to 238 were considered by Pearlstein [134] to illustrate the general characteristics of the neutron emission spectra.

In Figures 1.33 and 1.34, two examples of measurements of double differential neutron production cross sections at the Los Alamos *WNR* facility by Amian et al. [129, 130] (in angles 30°, 60°, 120°, and 150°) by 800 MeV protons on targets of Fe and Pb are shown. More details of these experiments are given in Part 2. The cross-section curves are seen to be very much alike, showing a broad maximum at ∼2–3 MeV, followed by a rapid fall of about above ∼20 MeV. The two different main components in the spectra are attributed to evaporation neutrons dominating the range below ∼20 MeV, and the cascade neutrons governing the shape above ∼20 MeV. The double differential cross sections are increasing with increasing target mass over the entire energy range and for all neutron emission angles. It can be seen from these examples that the cross sections below about 20 MeV for all angles widely coincide, indicating an almost *isotropic* neutron emission. In contrast to the evaporation region, the neutron production cross sections in the cascade region are strongly angular dependent, and forward peaking is evident. While the cross sections around 20 MeV are still of about the same order for all angles, the cascade component tails off rapidly, increasing with increasing emission angle. The general features of the angular dependent cross sections – their *anisotropy* – are qualitatively very similar for most of the target masses.

The total uncertainties of the experimental results presented here are determined by $\pm 1\sigma = 10$–15% and thus are of the order of the data point sizes. The above-shown experimental results are based on the so-called time-of-flight method (TOF), which will be described in more detail in Part 2 on page 289.

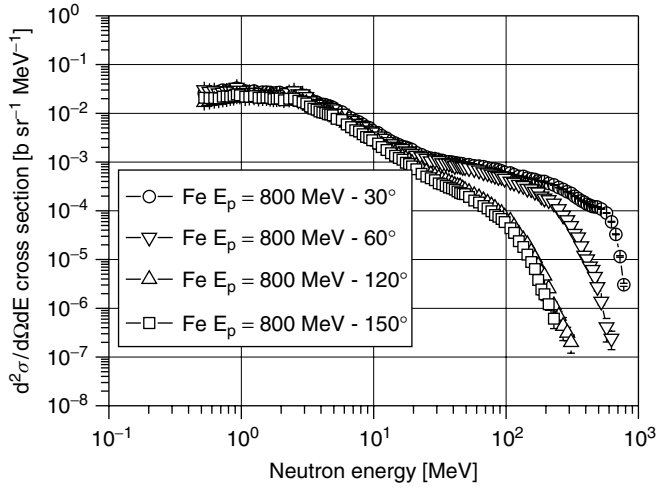

Fig. 1.33 Examples of proton (800 MeV) + Fe-induced experimental double differential neutron production cross sections at 30°, 60°, 120°, and 150° – measurements of Amian et al. [129, 130].

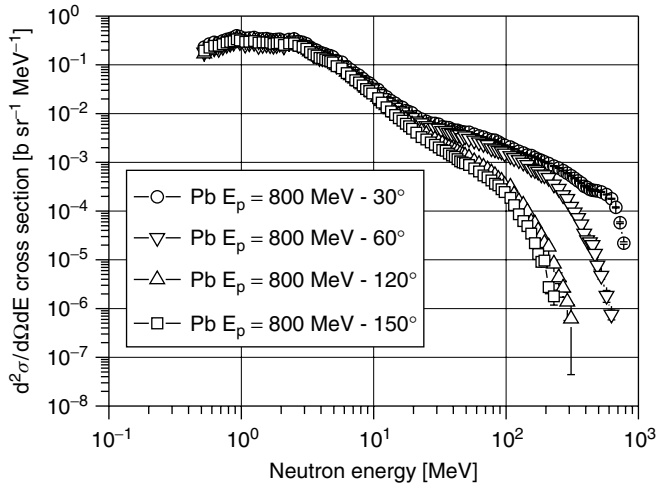

Fig. 1.34 Examples of proton (800 MeV) + Pb-induced experimental double differential neutron production cross sections at 30°, 60°, 120°, and 150° – measurements of Amian et al. [129, 130].

Although the neutron production channel in spallation collisions is the dominant one, other secondary particle production channels as the production of secondary protons, pions, or light charged, intermediate mass fragments (IMFs), and heavy residuals (cf. Figure 1.12 on page 19) are at least also important in model predictions and applications (cf. Part 2 on page 277 and Part 3 on page 495).

1.3.8
Hadronic–Electromagnetic Cascade Coupling

It should be noted that often both hadronic and electromagnetic cascades are important in the same problem whether the source is hadrons – protons or neutrons – or photons, electrons, and positrons. These processes are mainly a function of secondary particle production and their decay during the propagation of an intra- or internuclear-cascade in the target nucleus or in a so-called thick target, respectively. The ''coupling'' of hadronic and electromagnetic cascades may occur in the following way. The process may be initiated for example by either hadrons or leptons as incident particles on a target nucleus or a thick target:

starting with hadrons, e.g., protons or neutrons:

$$\begin{aligned} \text{proton/neutron} \quad + \quad & \text{nucleus/target} \\ & \longrightarrow \quad \pi^0 \longrightarrow 2\cdot\gamma \\ & \longrightarrow \quad \pi^{\pm} \longrightarrow \mu^{\pm} \longrightarrow e^{\pm} \\ & \longrightarrow \quad \mathrm{k}^0, \mathrm{k}^{\pm} \longrightarrow \mu^{\pm}, \pi^{\pm}, \pi^0 \longrightarrow e^{\pm}, \gamma \end{aligned} \tag{1.69}$$

starting with leptons, e.g., electrons or positrons:

$$\begin{aligned} \text{electron} \quad + \quad & \text{nucleus/target} \\ & \longrightarrow \quad \gamma, e^+, e^- \\ \gamma, e^{\pm} \; + \quad & \text{nucleus/target} \\ & \longrightarrow \quad \text{hadron–meson} \quad \text{cascade} \end{aligned} \tag{1.70}$$

The decay scheme and the particle properties have already been discussed in Section 1.2 in Eqs. (1.1) and in Table 1.1. A substantial fraction of the energy deposited in a hadron cascade is a direct result of electromagnetic cascades produced by the decay of neutral pions π^0 (mean life $\sim 10^{-16}$ s) into two photons, by low-energy photons produced during the intra- and internuclear evaporation process or by the decay of charged pions and muons. There is a large class of hadron cascade applications and issues which require the handling of *electromagnetic cascades*, their shower propagation, their energy deposition, and the production of hadrons and other secondary particles. The principal production processes during the development of *electromagnetic showers* (bremsstrahlung by production of electrons and positrons, pair production for photons) are well described by quantum electro dynamics (QED) theory.

It should be mentioned that at higher incident hadron energies the hadron production rate, e.g., for protons and neutrons, deviates from the linear rule due to the increase of π^0 production and the subsequent 2γ decay into the electromagnetic channel the so-called *electromagnetic drain* of the hadron cascade. As mentioned above, the mean half-life of π^0 is with $\sim 10^{-16}$ *s* very short; therefore, this fast

decay does not allow π^0 to take part in the internuclear cascade whereas the $\pi^{\pm}$ do. The $\pi^{\pm}$ decay time of 26×10^{-9} s is sufficiently long to allow further hadronic interactions once the $\pi^{\pm}$ are created. At higher incident energies above 10 GeV, other meson production channels will be opened which in addition deplete the cascade of energy.

Applications where such showers are observed are e.g., high-intensity spallation sources, high-energy physics calorimeters, shielding of accelerators, or the impact of space radiation on space vehicles. Details are given in Part 3 on page 495.

Besides the general way of spallation reactions induced by high-energy protons, hadron production, mainly neutrons, will also take place in target materials by electrons or bremsstrahlung photons. It should be noted that it is the photon interacting with the target material that releases the hadrons, rather than the direct interaction of the electrons. Several types of photonuclear interactions result in hadron production such as the so-called giant resonance production with photons of energy $E_\gamma \approx 10$–30 MeV, photodisintegration with photons of energy $E_\gamma \approx 50$–100 MeV, and photopion absorption with photons of E_γ about ≥ 140 MeV.

Figure 1.35 shows for small incident photon energies the giant-resonance peaks for Cu and Pb and above the pion production threshold of about 200 MeV the photo–pion production cross section as the average of proton and neutron. Above 140 MeV, the cross section for photons on nuclei rises again, opening the channels for photopion production. The cross section is characterized by a number of resonance peaks below and above of about 1 GeV which are caused by nucleon isobar formation (see Section 1.3.5.3). Between these two energies, e.g., 10 and

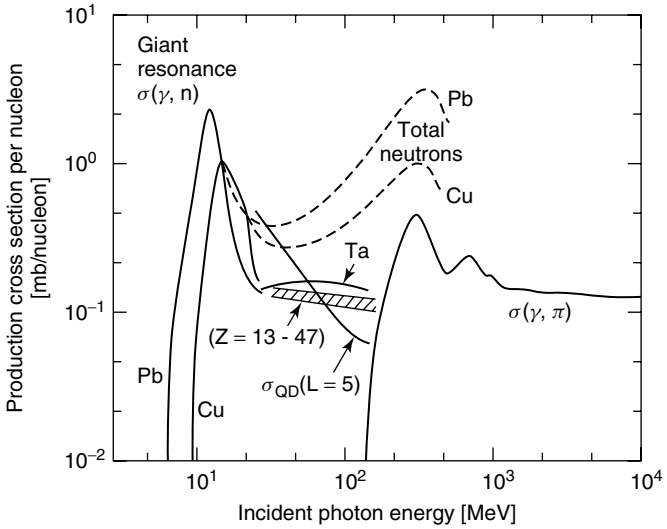

Fig. 1.35 A qualitative picture of the photoneutron production mechanism given as the cross section per target nucleon as a function of the incident photon energy (after Swanson [135]).

100 MeV, the behavior for medium Z-targets is shown as hachures [136], and a calculation for Ta [137] based on a intranuclear cascade model. Also shown for this energy region is the photoneutron cross section derived from a simple quasideuteron model, assuming $N = Z = A/2$, $L = 5$, where A, Z are for the target nucleus, and L is a dimensionless coefficient (Eq. (1.71)). The quasideuteron effect above the giant resonance is the remaining dominant neutron production mechanism in which the photon interacts initially with a neutron–proton pair within the nucleus, rather than with the nucleus as a whole, hence the name quasideuteron. As Figure 1.35 shows, this cross section is an order of magnitude below the giant-resonance peak. The cross section is related to the deuteron photodisintegration cross section $\sigma_D(E)$, qualitatively given by [138]

$$\sigma_{\mathrm{QD}}(E) \simeq L \cdot \frac{NZ}{A} \cdot \sigma_D(E), \tag{1.71}$$

where N, A, and Z refer to the target nucleus, and L (between 3 and 13) is a dimensionless coefficient as a measure of the probability that a neutron–proton pair is within a suitable interaction distance relative to the deuteron [139]. The overall effect is to add a tail of higher energy neutrons to the giant-resonance spectrum.

Electrons and positrons lose their energy by ionization as charged particles do. However, because of their small mass, they have significant losses also due to the production of radiation. For lead, the fractional energy loss due to bremsstrahlung exceeds that due to ionization for electron energies above 10 MeV, which is shown in Figure 1.36. Other significant energy loss mechanisms are elastic scattering described by the Bhabha differential cross section for electrons and the Møller formula for positrons, and positron annihilation. The dominant energy losses for high-energy electrons are bremsstrahlung and pair production which lead to the production of electromagnetic radiation or electromagnetic showers by the motion of electrons and positrons through matter. The well-known physical processes are described in detail standard textbooks such as, e.g., in Ref. [140]. Electrons and positrons have similar electromagnetic interactions in matter. Figure 1.36 shows the fractional energy loss per radiation length in Pb as a function of electron or positron energy. Electron and positron scattering is considered as ionization when the energy loss per collision is below 2.55 MeV, and as Møller or Bhabha scattering when it is above. At low energies electrons and positrons lose energy essentially by ionization, although other processes (Møller and Bhabha scattering, electron annihilation) contribute as shown in Figure 1.36. The ionization losses decrease exponentially with energy, bremsstrahlung losses rise nearly linearly (the fractional loss is nearly independent of energy), and dominates above a few tens of MeV in most materials.

The radiation length X_0, usually measured in (g/cm^2), has been calculated by Tsai [141] and is provided by an approximation formula in Ref. [19].

$$X_0 = \frac{716.4 \cdot A}{Z \cdot (Z+1) \cdot \ln(287/\sqrt{Z})} \left(\mathrm{g\,cm^{-2}}\right), \tag{1.72}$$

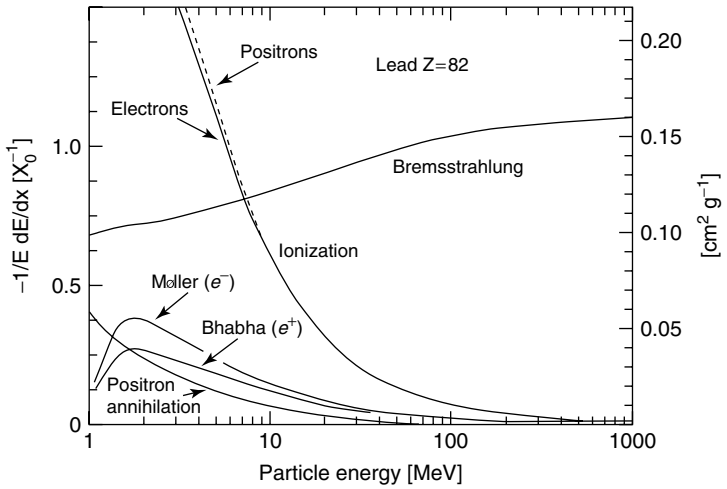

Fig. 1.36 Fractional energy loss per radiation length X_0 in lead as a function of electron or positron energy (after Yao et al. [19]).

Tab. 1.16 Calculated radiation lengths X_0 of Be to U using Eq. (1.72).

Medium	Z	A	Radiation length (g cm^{-2})
Be	4	9.01	65.19
C	6	12.01	42.70
Al	13	26.98	24.01
Fe	26	55.85	13.84
Cu	29	63.55	12.86
Ta	73	180.95	6.83
W	74	183.84	6.76
Au	79	196.97	6.42
Hg	80	200.59	6.39
Pb	82	207.2	6.31
U	92	238.03	6.00

where A and Z for the target material. In Table 1.16 calculated radiation lengths X_0 are given for some materials using Eq. (1.72).

It should be mentioned that the basic features of the energy loss already discussed for heavy particles in Section 1.3.6 are also valid for electrons and positrons, but the Bethe–Bloch formula (1.27) must be modified for several reasons: Electrons and positrons have a relatively small mass compared to heavy charged particles, at small incident energies the total energy loss is also determined by bremsstrahlung losses, and for electrons and positrons the collisions take place between identical particles, which lead to a indistinguishability. Also positron annihilation must be taken into

account ($e^+ + e^- \rightarrow \gamma + \gamma$). A modified Bethe–Bloch formula for ($e^+ + e^-$) can for example be found in Ref. [140]

As already discussed during the 1980s in Ref. [142], high power target systems of spallation sources or high-intensity proton accelerators are at the same time a source of charged pions and muons which decay into neutrinos ν and antineutrinos $\overline{\nu}$. Thus, such facilities can also provide a source for neutrino research in a so-called *neutrino factory*.

There are currently two kinds of intense neutrino of factories discussed.

1 The neutrino production mechanism from pions and muons: The mesons $\pi^{\pm}$ decay via the weak interaction with an average lifetime of about $\tau = 2.55 \times 10^{-8}$ s in leptons:

$$\begin{aligned} &\pi^+ \longrightarrow \mu^+ + \nu_\mu \quad (\text{branching ratio} = 99.9877\%) \\ &\quad \text{or} \\ &\pi^+ \longrightarrow e^+ + \nu_e \quad (\text{branching ratio} = 1.2 \times 10^{-4}\%) \\ &\quad \text{and} \\ &\pi^- \longrightarrow \mu^- + \overline{\nu}_\mu \quad \text{or} \quad \pi^- \longrightarrow e^- + \overline{\nu}_e . \end{aligned} \tag{1.73}$$

Muons $\mu^{\pm}$ have an average lifetime of about $\tau = 2.2 \times 10^{-6}$ s and decay via the following scheme:

$$\begin{aligned} &\mu^- \longrightarrow e^- + \overline{\nu}_e + \nu_\mu \\ &\quad \text{and} \\ &\mu^+ \longrightarrow e^+ + \nu_e + \overline{\nu}_\mu \quad (\text{branching ratio} \approx 100\%) . \end{aligned} \tag{1.74}$$

2 The decay of stored β-active emitters instead to produce neutrinos via the decay of pions and muons: The neutrino production with such emitters as ${}^{6}_{2}\mathrm{He}$ and ${}^{18}_{10}\mathrm{Ne}$ is as follows:

$$\begin{aligned} &{}^{6}_{2}\mathrm{He} \longrightarrow {}^{6}_{3}\mathrm{Li} + e^- + \overline{\nu}_e, \ (\text{with a half-life} \quad T_{1/2} = 0.8\,\mathrm{s}) \\ &\quad \text{and} \\ &{}^{18}_{10}\mathrm{Ne} \longrightarrow {}^{18}_{9}\mathrm{F} + e^+ + \nu_e, \ (\text{with a half-life} \quad T_{1/2} = 1.7\,\mathrm{s}) . \end{aligned} \tag{1.75}$$

The physics applications of the neutrino research are primarily neutrino oscillation physics and CP violation studies, but also measurements of cross sections of neutrino nucleus interactions.

An example of a spallation neutron source for neutrino research is the KARMEN experiment at the Rutherford Laboratory (The KArlsruhe Rutherford Medium Energy Neutrino Experiment) [143]. Other projects on neutrino factories can be found in Refs. [144, 145] and references therein. Experiments at existing spallation sources and the production of different parent ions for neutrino beams will be discussed in Part 3 on pages 585 and 638.